The Thesis Committee for Jake Andrew Haley
Certifies that this is the approved version of the following Thesis

On the Axial Crushing and Failure of Aluminum Alloy Tubes: Experiments and Numerical Simulations

APPROVED BY
SUPERVISING COMMITTEE:

Stelios Kyriakides, Supervisor

On the Axial Crushing and Failure of Aluminum Alloy Tubes: Experiments and Numerical Simulations

by

Jake Andrew Haley

Thesis

Presented to the Faculty of the Graduate School of
The University of Texas at Austin
in Partial Fulfillment
of the Requirements
for the Degree of

Master of Science in Engineering

The University of Texas at Austin
May 2020

Dedication

To my family.

Acknowledgements

I am thankful for all of the contributions from my advisors, professors, and colleagues during this academic process. First, I would like to express my thanks to my advisor, Dr. Stelios Kyriakides, for his encouragement and support during my time at the University of Texas. His expertise and guidance were integral to this work. I would also like to thank Dr. K. Ravi-Chandar for discussions of dynamic experimental methods, data acquisition, and for co-reading this thesis.

I'd like to especially thank Kelin Chen and Martin Scales for their diligent work to calibrate the constitutive models used in this study. Thanks to the ASE/EM staff: Scott Messec, Traci Laird, Joe Pokluda, Pablo Cortez, and Steve Sanders. Special thanks to Joe Pokluda for his expert machining and teaching that was fundamental to the experimental work. Thanks to the Texas Advanced Computing Center (TACC) for the use of the Lonestar5 supercomputing system. I would also like to thank my fellow graduate students Solon Tsimpoukis, Weihan Zhang, Chenglin Yang, Martin Scales, Kelin Chen, Karlos Kazinakis, Harvey Fulton, and Juan Suarez-Domit for their advice, troubleshooting chats, and friendship during my time here. I'd also like to thank my family, friends, and, in particular, Holly, for being supportive of moving away to pursue this goal. My education and research were made possible by the financial support from the National Science Foundation GOALI grant CMMI-1663269 and the University of Texas at Austin.

Abstract

On the Axial Crushing and Failure of Aluminum Alloy Tubes: Experiments and Numerical Simulations

Jake Andrew Haley, M.S.E.
The University of Texas at Austin, 2020

Supervisor: Stelios Kyriakides

The use of aluminum alloys for light-weighting purposes in energy absorbing components of automobiles is hindered by the relatively low ductility and more complicated constitutive behavior of these alloys. This study presents results from series of quasi-static and dynamic axial crushing experiments on extruded Al-6061-T6 circular tubes of varying *D/t* ratios. A custom drop-weight testing facility was used to perform the dynamic experiments. Crushing led to axisymmetric, mode-2, and mode-3 concertina folding. In the quasi-static experiments, the folding was monitored using time-lapse photography; dynamic crushing was monitored using high-speed photography. The crushing responses and energy absorption capacities are evaluated and failures were recorded. Failure was observed in most of the experiments with the severity depending on the *D/t* and mode of folding.

The experiments are simulated with three-dimensional, nonlinear finite element analysis using the von Mises, the non-quadratic Hosford, and the calibrated anisotropic Yld04-3D models. The Yld04-3D model was found to most accurately reproduce the structural response under both quasi-static and dynamic loadings. This model was used to the monitor the strains induced in two example cases: axisymmetric folding under quasi-static loading, and mode-2 folding under dynamic loading. The analysis predicted maximum strains to develop at locations on the model tube where failure is observed on the specimen in the experiments. It is concluded that the Yld04-3D constitutive model is most suitable for the prediction of the structural response and failure in tube crushing of this aluminum alloy.

Table of Contents

Chapter 1: Introduction

The development of lightweight and effective energy absorbing structures has recently received increased interest from the automobile industry. Industry is now obligated to follow tighter fuel-efficiency and crashworthiness standards as required by federal agencies such as the National Highway Traffic Safety Administration (NHTSA, 2015). Additionally, the advantages of new features brought about by stricter rules have become attractive marketing incentives to customers. In order to satisfy the increasing demands of fuel efficiency and safety, the traditional body-on-frame steel structure is being replaced by a unibody construction using lighter materials such as high-strength steel, aluminum alloys, and composites (Krome, 2018).

The use of aluminum as an alternative to steel is challenging because of its lower ductility and higher cost. Alternative designs and new alloys have made the use of aluminum a viable alternative to steel in the automotive industry; today, all-aluminum cars and trucks are available from many manufacturers (Ayapana, 2015). The alternative unibody frame design utilizes several extruded aluminum tubes in place of traditional stamped and spot-welded steel tubes. The frame design incorporates *crumple zones* that consist of extruded aluminum parts acting as energy absorbing structures. For example, Fig. 1.1a shows an extruded tubular aluminum front rail used in automobile frames (Kohar et al., 2017). Under impact, such components are designed to act as energy absorbers and simultaneously mitigate the impact force transferred. These goals are achieved by concertina folding of the thin-walled compartments of the cross section. This folding is hampered by the low ductility of aluminum, causing ruptures, tears, and possibly catastrophic failures. For example, the rail in Fig. 1.1a formed the expected energy absorbing folds when crushed under impact, but also developed many tears (see Fig. 1.1b). These tears can lead to catastrophic failures that limit the energy absorbing capacity of the component. Such failures need to be determinedly avoided. This prompted more extensive investigations into the development of constitutive models and failure criteria for aluminum alloys. Careful crushing experiments are concurrently used to evaluate these models. To this end, the present study used tube crushing experiments to evaluate recently developed constitutive models for Al-alloys.

1.1 REVIEW OF TUBE CRUSHING

The axial crushing of closed-section circular tubes to understand and predict their energy absorption characteristics is a recurrent structural mechanics problem that has been thoroughly examined by many, including Alexander (1960), Abramowicz and Jones (1984), Singace et al. (1995, 1999), Weirzbicki et al. (1992), among others. Bardi et al. (2003) reviewed this body of work and their findings can be summarized as follows: Experiments were conducted on tubes of different metal alloys under both static and dynamic axial loading conditions. It was found that tubes with lower diameter-to-thickness ratios (*D/t*) develop axisymmetric concertina folds (e.g., see Fig. 1.2a). For higher *D/t* values folding tends to feature two or three circumferential waves called mode-2 or mode-3, respectively (see Fig. 1.2b for mode-3 folding). Furthermore, it was noted that the tubes can begin crushing in one mode and switch to a different mode as the crushing progresses. Several complementary plastic hinge models were developed which predict the mean crushing stress quite accurately and the energy absorbed per unit length with less accuracy.

1.2 REVIEW OF NUMERICAL EFFORTS

In recent years, finite element analysis has been employed to predict tube crushing with much improved accuracy (e.g., Bardi et al., 2003). More generally, finite element analysis has been an effective tool in the numerical prediction of the energy absorbing characteristics of structures (e.g., Kazancı and Bathe, 2011; Kohar et al., 2017). However, numerical prediction of failure of aluminum thin-walled structures is complicated by the following: It has been established that predictions of large deformations of aluminum can be heavily influenced by the adopted constitutive model. In addition, material anisotropy that is introduced by the manufacturing process places increased demands on the modeling. Suitable anisotropic constitutive models require calibration via extensive experiments coupled with analysis (e.g., family of models by Barlat for Al-alloys). Furthermore, the material stress-strain response to large deformations is essential. Tensile specimens neck at relatively low strain levels. Thus, the hardening response must be extrapolated numerically from the force-elongation response using inverse procedures (see Giagmouris et al., 2010; Tardif et al., 2012; Kohar et al., 2017; Chen et al. 2015, 2019; Scales et al. 2019). Most recently, Chen et al. (2019) calibrated the Yld04-3D non-quadratic, anisotropic constitutive model of Barlat et al. (2005), and showed it to be more suitable for numerical prediction of large deformation and failure in extruded Al-6061-T6 tubes.

1.3 SCOPE OF THIS WORK

The present investigation involves first an experimental study on the axial crushing of extruded circular Al-6061-T6 tubes. Chapter 2 presents a carefully designed experiment series on pairs of nearly-identical specimens in which the first is crushed under quasi-static loading and the second is tested under impact. The experiment goals are to measure the two crushing responses and establish any differences between quasi-static and dynamic loadings. Of interest are also the types of failure induced by concertina, mode-2, and mode-3 crushing modes.

The quasi-static and dynamic crushing experiments are subsequently simulated numerically using nonlinear finite element analysis. Here, among other issues, the effect of the adopted constitutive model on the responses and induced strains is investigated. Chapter 3 contains the details of the von Mises, Hosford-8, and Yld04-3D constitutive models used in this study. Chapter 4 discusses the model construction and the discretization of its 3-D geometry for the quasi-static and dynamic simulations using the explicit LS-Dyna code. The strains predicted at locations on the tubes where failure is observed experimentally are paid special attention. Finally, conclusions drawn from the study are presented in Chapter 5.

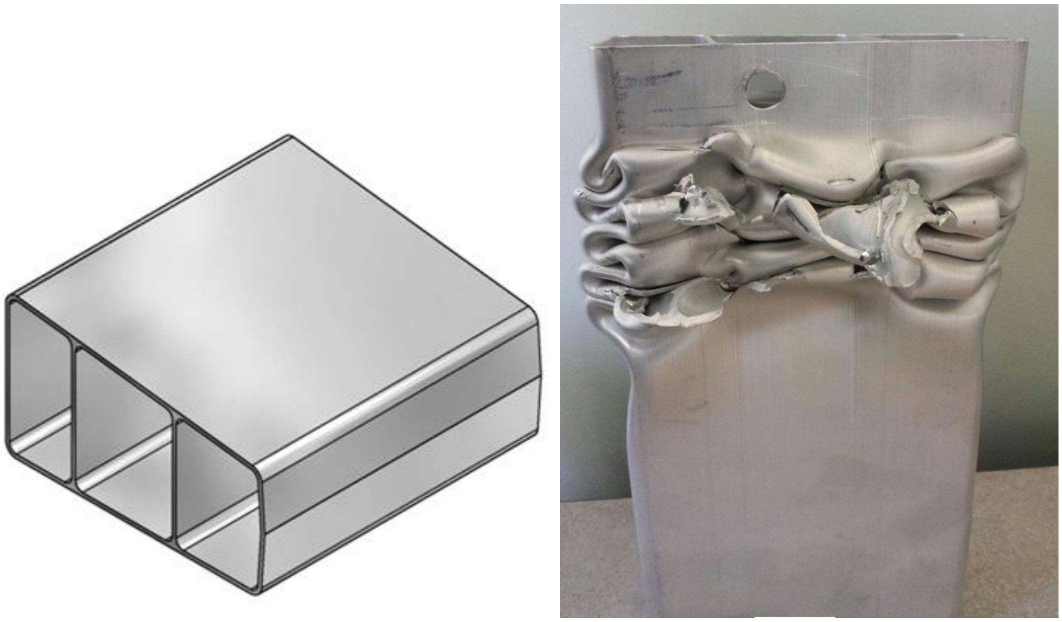

(a) (b)

Fig. 1.1: (a) Cross-section of extruded aluminum front rail design.
(b) Crushed image of front rail exhibiting severe failures.
(courtesy Kohar, 2017).

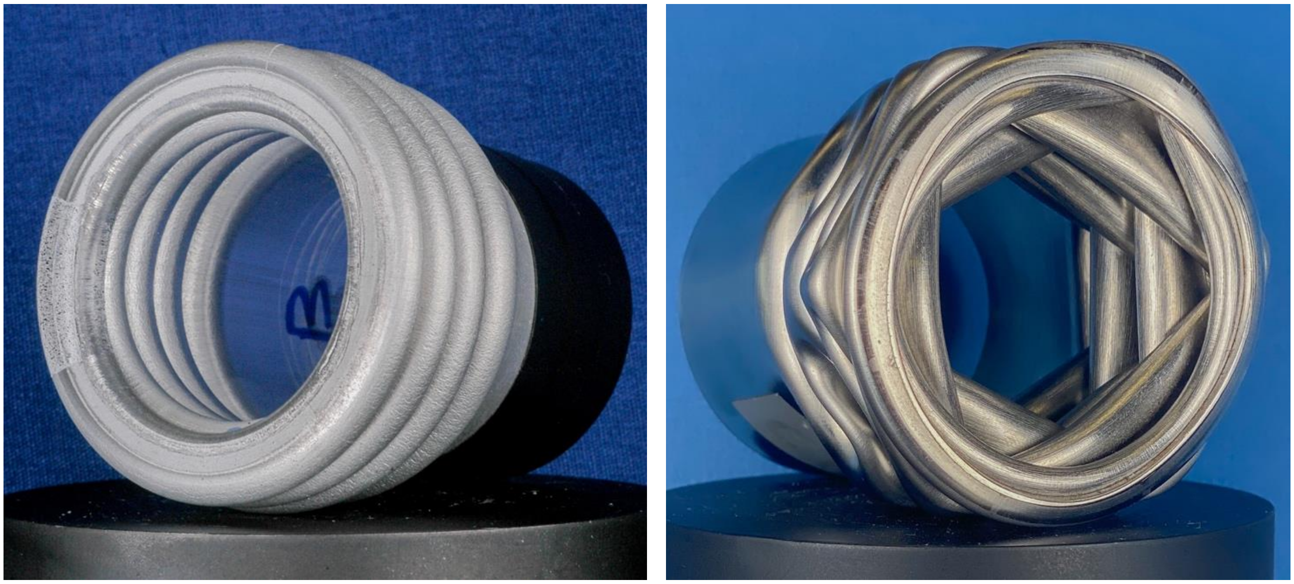

(a) (b)

Fig. 1.2: Modes of tube crushing: (a) Axisymmetric concertina folding of an Al-6061-T6 tube. (b) Mode-3 folding of a stainless-steel tube.

Chapter 2: Tube Crushing Experiments

The concertina-type axial crushing of commercially available Al-6061-T6 tubing is examined experimentally. A series of quasi-static and dynamic axial crushing experiments were performed on thin-walled tubular specimens with varying *D/t* ratios. The specimens were machined out of seamless, extruded, commercially available Al-6061-T6 stock tubing with nominal outer diameter of 2.0 in (50.8 mm) and 0.1875 in (4.76 mm) wall thickness. This chapter contains details of the fabrication of the specimens, testing configurations, data acquisition, data processing, and experimental results.

2.1 SPECIMEN FABRICATION, MEASUREMENT, AND PREPARATION

The specimens had an overall length of approximately 5.5 in (140 mm). A 4.3 in (109 mm) test section of thickness *t* was machined on the outer surface to allow for development of folds during crushing. The excess material was removed in a lathe by centering the tube using solid, tight-fitting ID plugs. Special care was taken to ensure that the specimen ends were square. The remaining length of 1.125 in (28.6 mm) was turned down to a diameter of 1.825 in (46.4 mm) and used to grip the specimen. A specimen schematic is shown in Fig. 2.1.

After fabrication, the specimen diameter *D*, thickness *t*, and initial test section length *L* were measured at evenly spaced circumferential increments at both ends of the test section. The average values of *D*, *t*, and *L* were recorded and an estimate of the wall eccentricity X_o was calculated as follows:

$$X_o = \frac{t_{\max} - t_{\min}}{t_{\max} + t_{\min}}. \tag{2.1}$$

A summary of *D*, *t*, and *L* and Ξ_o are given in Tables 2.1 and 2.2 for quasi-static and dynamic specimens, respectively.

For a select number of experiments the local strain in the folds was monitored using digital image correlation (DIC). Thus, a speckle pattern was painted on a strip with an angular span of 45° along the full length of the test section. A thin layer of matte grey spray paint was added in areas away from the DIC speckle strip to reduce the glare from the external lighting, as described in a later section. If the experiment did not feature DIC, the matte grey paint was painted over the entire surface of the specimen.

2.2 EXPERIMENTAL CONFIGURATIONS

2.2.1 Quasi-Static Experiments

Quasi-static crushing experiments were performed using an MTS servo-hydraulic machine under displacement control. The specimen was mounted onto the machine using a custom-designed gripping facility while the other end made simple contact with a hardened steel plate as shown in Fig. 2.2. A solid end-plug was first inserted into the gripped end of the tube. It was then placed into the grip that consisted of a *Ringfeder* clamp and solid spacers. The inner plug and spacers were custom fabricated with tight dimensional tolerances to ensure quality alignment with the contact plate.

The tubes were crushed at a displacement rate of $\dot{\delta}_1 = 8\times 10^{-4}$ in/s (0.0203 mm/s) past the initial load peak, and then the rate was increased to $\dot{\delta}_2 = 1.33\times 10^{-3}$ in/s (0.0338 mm/s) until the end of the experiment. Photographs were taken at a time interval of one image every 4 s for $\dot{\delta}_1$ and then one image every 8 s for the rest of the test. The load (P), displacement (δ), and images were recorded on a common time (T) base via a LabVIEW VI and a National Instruments DAQ module.

Post-processing and data analysis were handled with Python's SciPy and MatPlotLib modules concurrently with Microsoft Excel. The raw data was filtered with a Savistky-Golay linear data filter to remove noise from the captured data. Each photo's write time was extracted from the OS and interpolated against the experiment time in order to associate each photo to a particular point along the P-δ response. The final result is a P-δ response with a photo corresponding to each data point.

2.2.2 Dynamic Experiments

A series of dynamic axial crushing experiments were conducted using a drop-weight test facility alongside the quasi-static experiments. Specimens were made in pairs with special care so that the quasi-static and dynamic specimens had nearly identical dimensions. The experimental set-up is shown schematically in Fig. 2.3 in which the various components are labeled. The drop tower has a height of 11 ft (3.35 m) and consists of three 1.5 in diameter case-hardened guide rails. A chosen number of 25 lb steel disk weights are mounted on a yoke that loosely connects to three bushings with linear bearings. The yoke carries a hardened steel impact plate that contacts the specimen. The assembly is raised to the drop height via an electric winch. It can be released by pulling on a cord that is connected to quick-release snap shackle. The required kinetic energy is chosen by the number of weights used and the drop height.

The specimen is mounted in a special housing as shown in Fig. 2.4. It is in contact with a lower plate that transfers the force of impact to an integrated electronics piezo-electric dynamic force sensor (Dytran 1061v6) that is rated to 50,000-lbf (222 kN) in compression. The load cell is encased in a heavy circular housing and kept loosely in place by set screws. The bottom end of the specimen is gripped in a similar manner as in the quasi-static crushing experiments. Here, the clamp, the spacer, and the specimen with the solid inner plug are enclosed by a thick outer ring as shown in Fig. 2.4.

The load cell signal was continuously monitored via a National Instruments high-speed data acquisition system. The data acquisition system consisted of a PXI-1042Q chassis, an 8-channel PXI-6123 acquisition card, and a NI-PXI-8196 PC running LabView software (NI DAQ). The system was set to record at a rate of 500 kHz with a 16-bit resolution channel. The system continuously records data and saves when the signal reaches a defined trigger voltage set by the user in the LabView VI. The software was set to save data 40 ms before the trigger event and 160 ms after. 100k data points were captured over this period.

The crushing event was also monitored with a Photron high-speed camera and its proprietary Fastcam Viewer 3 software. The camera was run at 10,000 frames/s and the pixel resolution was set at 384x688. The high-speed camera is also continuously recording and saves a 1.5 s span of images when a trigger is received. The camera trigger is sent with a Tektronix DPO3034 oscilloscope that is monitoring the same load cell signal as the NI DAQ. The trigger voltage level is the same as the NI DAQ so that the images and data are recorded on a common time (T) basis. The camera trigger is set at the center of a 1.5 s span so that images before and after the crushing event are recorded. The capture settings resulted in approximately 200 images of the collapse event. Fig. 2.5 shows a block diagram of the data acquisition and triggering systems of the dynamic crushing experiments.

For the high-speed camera set-up, an array of lights surrounding the specimen provided the required light intensity for the chosen camera settings. The lights were turned on immediately before and after each test in order to avoid overheating any components of the experiment. Fig.

2.6 shows a photograph of the weight assembly, the clamped specimen, the high-speed camera, and the lights.

The weight assembly was dropped from a height of approximately 10.5 ft (3.2 m) in all experiments. This resulted in a maximum velocity of approximately 25 ft/s (7.62 m/s). The mass added to the drop weight assembly for each dynamic experiment was determined by equating the measured crushing energy in the corresponding quasi-static experiment to the required kinetic energy.

Again, Python's SciPy, MatPlotLib, and Microsoft Excel were used for data processing. The raw data load cell data was filtered with a Butterworth analog low-pass filter to remove extraneous noise. GOM Correlate DIC was used to edge track a point on the hardened steel impactor on the falling rig. This edge tracking process gave δ-T data. The P-T data from the load cell and the δ-T response from the image series were interpolated on the common time base to generate a P-δ response.

2.3 EXPERIMENTAL RESULTS

2.3.1 Quasi-Static Experiment Results

Results from a typical experiment, CR14 with $D/t = 20.5$, will be used to describe the quasi-static crushing behavior (see Table 2.1). The tube collapse began near the steel plate and developed four axisymmetric folds (n0-4 in Table 2.1). The recorded P-δ response, normalized by the yield load P_o and the tube diameter D, is shown in Fig. 2.7 and a set of corresponding photographic images in Fig. 2.8.

The P-δ response initially exhibits a stiff elastic trajectory and then softens as the material begins to yield and soon reached a maximum. Frictional contact with the top plate provides enough constraint for the structure to localize into an *elephant foot* axisymmetric bulge as shown in image ① (e.g., see Bardi et al., 2003). Beyond the maximum, the load drops precipitously (②). As the load continues to drop, the bulge collapse further forming in a ǀ -shape until its upper, outer surface makes contact with the steel plate (image ③). The structure locally stiffens causing the load to rise again. A second load maximum is achieved, the load drops somewhat until the inner surfaces of the ǀ -shaped lobe make contact at the valley near station ④. The first lobe has fully formed after the inner contact occurs and loading resumes (④).

The load rises to a third peak and drops again near δ/D = 0.4 indicating the start of development of the second lobe as seen in image ⑤. Formation of the second lobe hastens as the response drops to station ⑥. The valley after station ⑥ is the point where the outer, upper surface of the second lobe makes contact with the outer, lower surface of the first lobe. The structure then goes through similar two-peak action as ③-⑥. This starts at the second deep valley and continues to station and image ⑨. This includes the completion of the second lobe and the formation and completion of the third lobe. The secondary peak of the cycles reduces its amplitude from the first to the second cycle and disappears third cycle.

If observed closely, the image series shows a nearly axisymmetric looking collapse throughout the entire experiment, but a small amount of asymmetry is visible in image ⑨ of Fig. 2.8. The right side of the lobe has not fully made contact while the left side has. This progressive loss of symmetry may be due to imperfect rigid plate contact at the onset of crushing.

The in-plane deformation, hoop strain ε_θ, was monitored using 2-D DIC on the image series captured during the experiment. The recorded hoop strain is plotted against the crushing displacement in Fig. 2.9. The strain tracking was terminated once the upper, outer surface of the first lobe contacted the rigid plate, as discussed previously (station ③ in Fig. 2.7). A corresponding set of images with a ε_θ color contour is overlaid on the experimental images in Fig. 2.10.

Fig. 2.11 shows images of the crushed specimen. The ‘orange peel’ effect that is typical of this aluminum alloy can be seen on the outer surface but no significant failure is visible. The specimen was cut in half axially and the flat edges were polished for observation. Fig. 2.12 shows a sectional view of the four folds that developed in this experiment. On the extrados of the lobe formed from the inside surface of the tube, significant failure can be observed (marked with red circles). In experiments with lower *D/t* ratios such as CR15, these failures are often much more significant and have completely torn through the thickness in certain experiments. During the formation of the first lobe, the top surface slides inward and the frictional contact rounds the edge off as shown at the top of Fig. 2.12. The green circle highlights the rounding of the initially square top edge.

A total of six quasi-static crushing experiments were performed for *D/t* ranging from 18.5 - 35.6. The main parameters of these experiments are summarized in Table 2.1. This table includes the geometric parameters discussed previously. In addition, the yield load P_o, limit load P_L, mean crushing load for the whole period $\bar{P}$, mean crushing load for two steady-state periods $\bar{P}_{2-3}$, and final crushing displacement δ_{cr} are listed. A more detailed definition of these parameters is given in Appendix A.

It is worth mentioning that in two of these experiments, CR12 and CR16, following two axisymmetric folds, the crushing switched to a mode-3 folding. A photograph of the specimen from CR16 is shown in Fig. 2.13. Here, there is significant failure observed in the later folds that can be seen to protrude inward in Fig. 2.13b.

2.3.2 Dynamic Experiments Results

Experiment DN4, with the same *D/t* as CR14, will be used to describe a typical dynamic crushing experiment. The dynamic crushing P-δ response, normalized by the yield load P_o and the tube diameter *D*, is shown in Fig. 2.14. The figure includes the velocity of the impactor. The impact velocity is about 25 ft/s (7.62 m/s). It initially decreases nearly linearly but drops off as the crushing is completed. The point of zero velocity corresponds to the point of maximum displacement at which point the structure begins to unload elastically.

Fig. 2.14 features a set of numbered stations that correspond to the set of images from the high-speed recording shown in Fig. 2.15. The response begins with a stiff, elastic region followed by yielding and a load maximum. Collapse starts at the top where frictional contact is made with the impactor. Similar to the quasi-static response, following the limit load deformation localizes into an axisymmetric bulge that can be seen in image ①. By station ②, the structure has gone through a similar two-peak axisymmetric collapse phase. As the response approaches station ③, it is clear from the corresponding image that axisymmetry is lost, as a buckling mode with 2 circumferential waves (mode-2) has appeared. This mode is seen at different stages of development in images ④, ⑤ and ⑥ which encompass a small and a large load peak. A second mode-2 fold begins to develop following the valley between stations ⑥ and ⑦. The crushing is terminated before the second mode-2 fold develops fully. Station ⑨ is the zero-velocity point of the weight assembly and the crushed tube unloads elastically. Unlike the axisymmetric folds, the strain history imposed by the non-axisymmetric modes lead to local failures that are apparent on the outer surface. The first visible sign of failure can be seen in image ④ where they are highlighted in yellow circles. In images ⑤ and ⑥, failure develops at additional sites and a tear appears in the upper right corner of the fold. Interestingly, as the second fold develops failures appear in similar locations on the outer of the new fold.

A clearer view of the outer surface failures is provided in a photograph of the crushed specimen in Fig. 2.16. The tear in the top right of the image is seen to be protruding covering the axisymmetric folds. This specimen was also sectioned axially and a cross-sectional view is shown in Fig. 2.17. Here the tear is seen to have affected the entire wall thickness. This section cut corresponds to the mid-width of the protrusion and has a counterpart at a diametrically opposite site. On both sides, the through-thickness tear covers the full width of the protrusion (see Fig. 2.16).

A total of six dynamic crushing experiments were performed for *D/t* ranging from 18.6 - 35.5. The main parameters of these experiments are summarized in Table 2.2. This table includes similar parameters to the quasi-static crushing experiments, and, in addition, the drop weight assembly mass *m* and the maximum velocity at impact, $V_{\max}$. Details of the crushing parameters are presented in Appendix A. None of the dynamic experiments collapsed in a fully axisymmetric fashion. For this reason, there is not a well-defined steady-state crushing response region and therefore $\bar{P}_{2-3}$ is not calculated (see Appendix A for discussion).

Mode switch occurred in all dynamic experiments. It is suspected to be caused by a small amount of misalignment between the impactor and the top of the specimen. The connection between the yoke and the housing of the three linear bearings is not rigid to allow for smoother sliding of the assembly; and this may allow a small amount of rocking of the impactor. The effect of this misalignment will be further discussed in Chapter 4 in light of numerical results.

Table 2.1: Main parameters for crushing experiment: Quasi-Static.

Exp. CR-	D in (mm)	t in (mm)	D/t	Ξ_o %	L in (mm)	P_o kip (kN)	$\frac{P_L}{P_0}$	$\bar{P}$ kip (kN)	$\bar{P}_{2-3}$ kip (kN)	δ_{cr} in (mm)	Mode/ Folds
11	1.7648 (44.83)	0.0685 (1.740)	25.8	2.5	4.230 (107.4)	15.1 (67.1)	1.03	9.3 (41.4)	8.8 (39.0)	2.397 (60.88)	n0-4.5
12	1.7240 (43.79)	0.0485 (1.232)	35.6	3.2	4.197 (106.6)	10.4 (46.4)	1.02	5.2 (22.9)	-	2.511 (63.78)	n0-2/ n3-2.5
13	1.7841 (45.32)	0.0780 (1.981)	22.9	1.7	4.216 (107.1)	17.4 (77.2)	1.05	11.9 (52.7)	11.2 (49.6)	2.523 (64.08)	n0-4
14	1.8036 (45.81)	0.0880 (2.235)	20.5	1.6	4.407 (111.9)	19.8 (88.1)	1.05	14.1 (62.5)	13.3 (59.2)	2.779 (70.59)	n0-4
15	1.8265 (46.39)	0.0988 (2.510)	18.5	1.5	4.194 (106.5)	22.5 (100.2)	1.07	17.9 (79.7)	16.5 (73.4)	2.650 (67.31)	n0-3.5
16	1.7479 (44.40)	0.0598 (1.519)	29.2	2.4	4.358 (110.7)	13.0 (58.0)	1.04	7.5 (33.5)	7.3 (32.3)	2.480 (62.99)	n0-2/ n3-2

Definitions of P_o, P_L, $\bar{P}$,$\bar{P}_{2-3}$, and δ_{cr} given in Appendix A

Table 2.2: Main parameters for crushing experiment: Dynamic.

Exp. DN-	D in (mm)	t in (mm)	D/t	Ξ_o %	L in (mm)	m lb (kg)	$V_{\max}$ ft/s (m/s)	P_o kip (kN)	$\frac{P_L}{P_0}$	$\bar{P}$ kip (kN)	δ_{cr} in (mm)	Mode/ Folds
1	1.7643 (44.81)	0.0683 (1.743)	25.8	2.4	4.285 (108.8)	150 (68)	24.9 (7.59)	15.0 (67.2)	1.11	7.6 (34.0)	2.125 (53.98)	n0-2/ n2-1
2	1.7230 (43.76)	0.0485 (1.232)	35.5	2.9	4.267 (108.4)	100 (45)	24.3 (7.41)	10.4 (46.4)	1.09	4.7 (21.0)	2.59 (65.79)	n0-2/ n3-2
3	1.7836 (45.30)	0.0782 (1.986)	22.8	1.3	4.211 (107.0)	250 (113)	24.7 (7.53)	17.4 (77.4)	1.18	9.8 (43.7)	2.09 (53.09)	n0-1/ n2-1.5
4	1.8009 (45.74)	0.0869 (2.207)	20.7	1.3	4.258 (108.2)	250 (113)	24.8 (7.56)	19.5 (86.9)	1.15	13.3 (59.1)	2.43 (61.72)	n0-1/ n2-2
5	1.824 (46.33)	0.0980 (2.489)	18.6	1.5	4.305 (109.3)	250 (113)	25.3 (7.71)	22.3 (99.2)	1.19	16.1 (71.7)	1.93 (49.02)	n0-1/ n2-1
6	1.7480 (44.40)	0.0601 (1.527)	29.1	2.7	4.236 (107.6)	150 (68)	24.3 (7.41)	13.1 (58.3)	1.17	7.4 (32.9)	2.54 (64.52)	n0-1/ n3-3

Definitions of P_o, P_L, $\bar{P}$, and δ_{cr} given in Appendix A

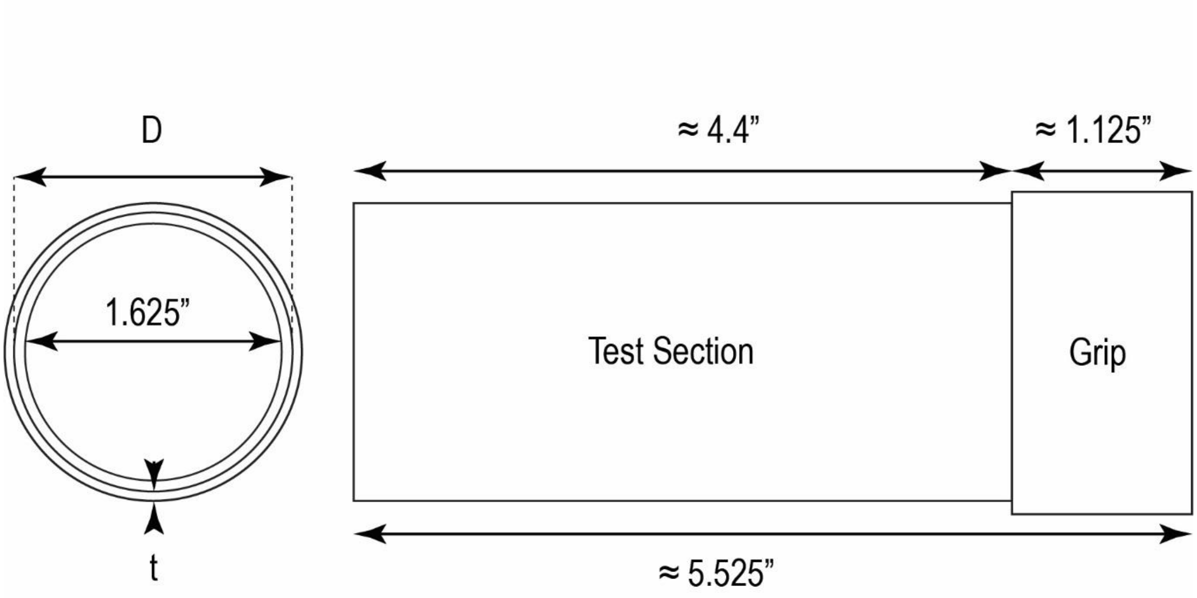

Fig. 2.1: Schematic of specimen for quasi-static and dynamic crushing experiments.

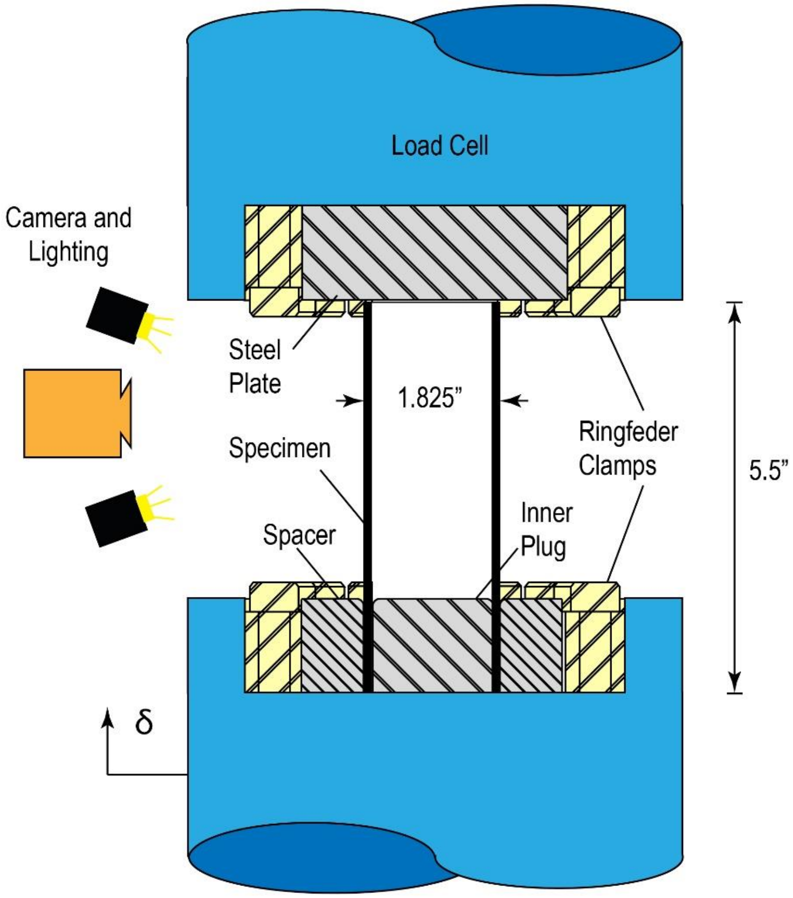

Fig. 2.2: Schematic of quasi-static crushing experiments.

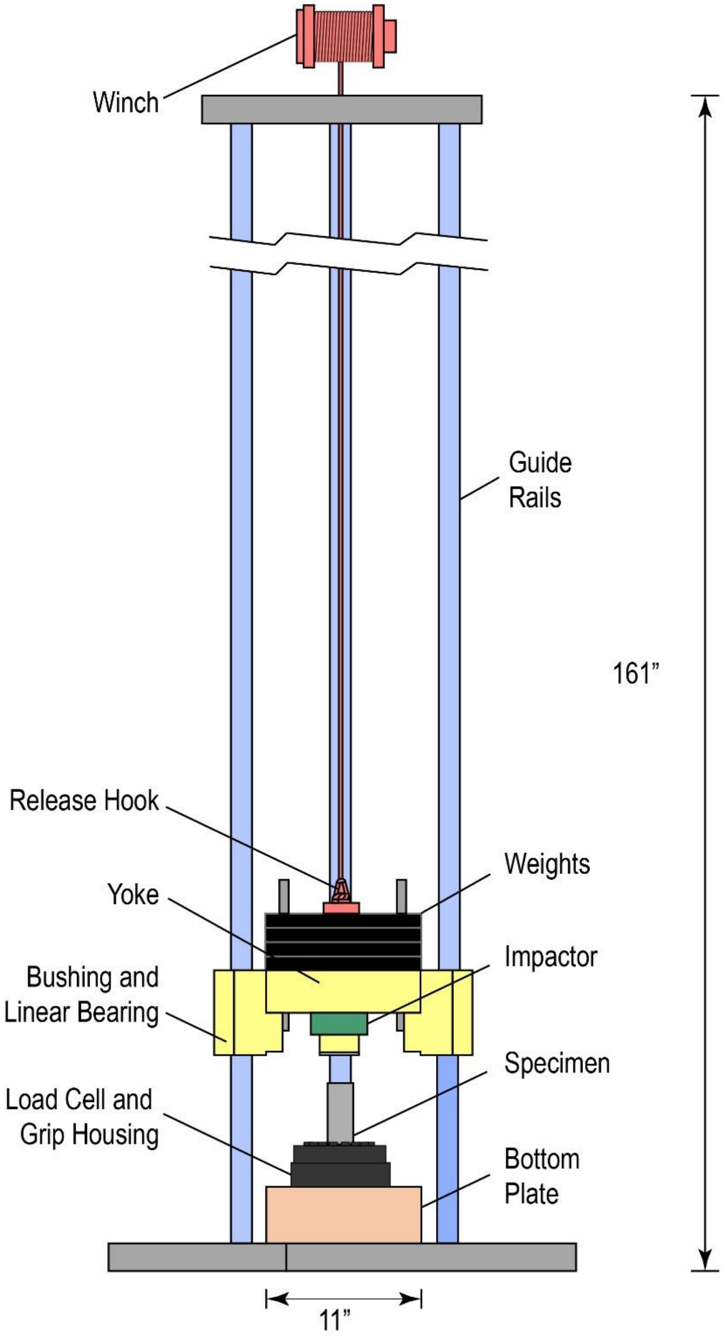

Fig. 2.3: Schematic of drop weight test facility for dynamic crushing experiments.

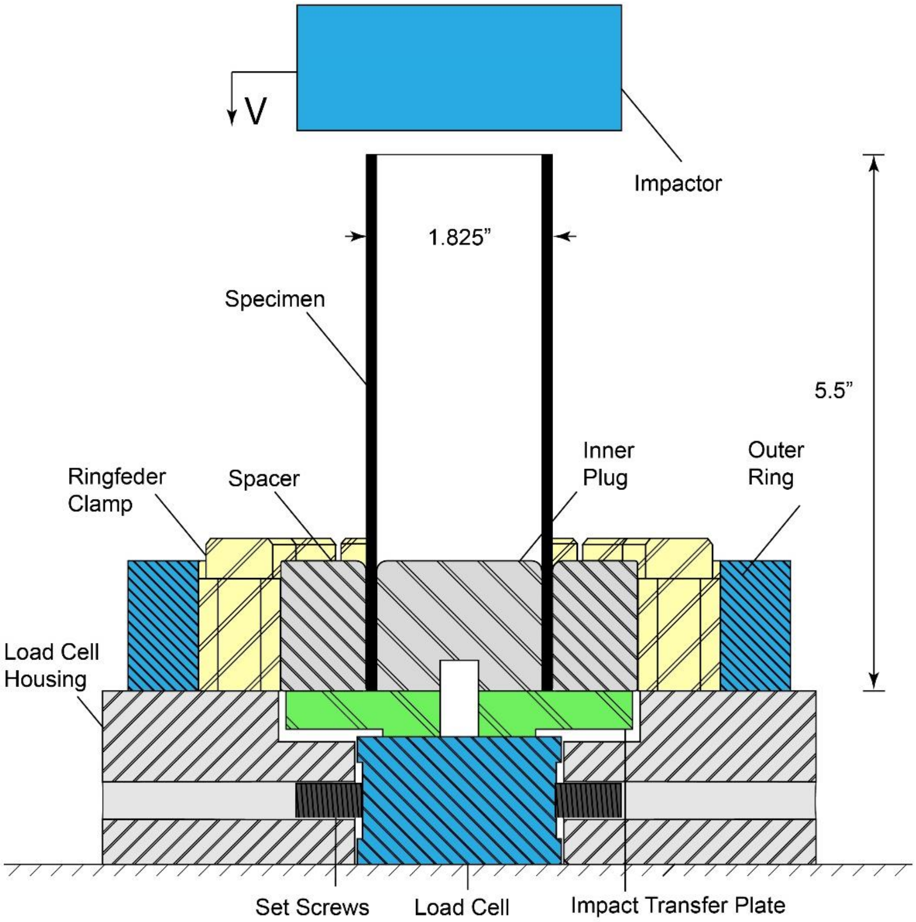

Fig. 2.4: Specimen housing for dynamic crushing experiments.

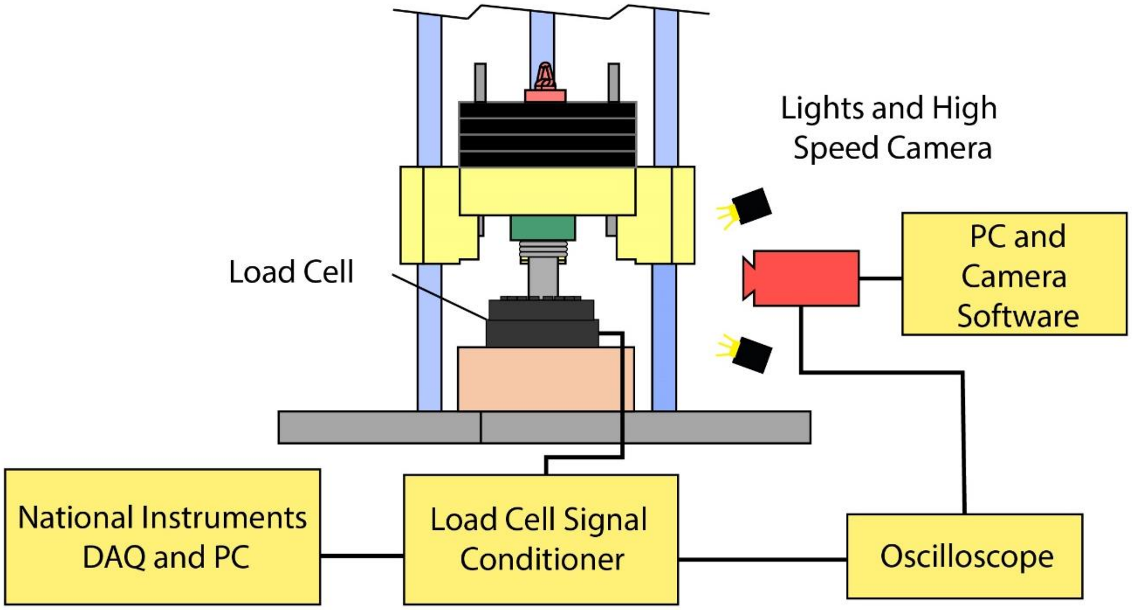

Fig. 2.5: Diagram of data acquisition and triggering for dynamic crushing experiments.

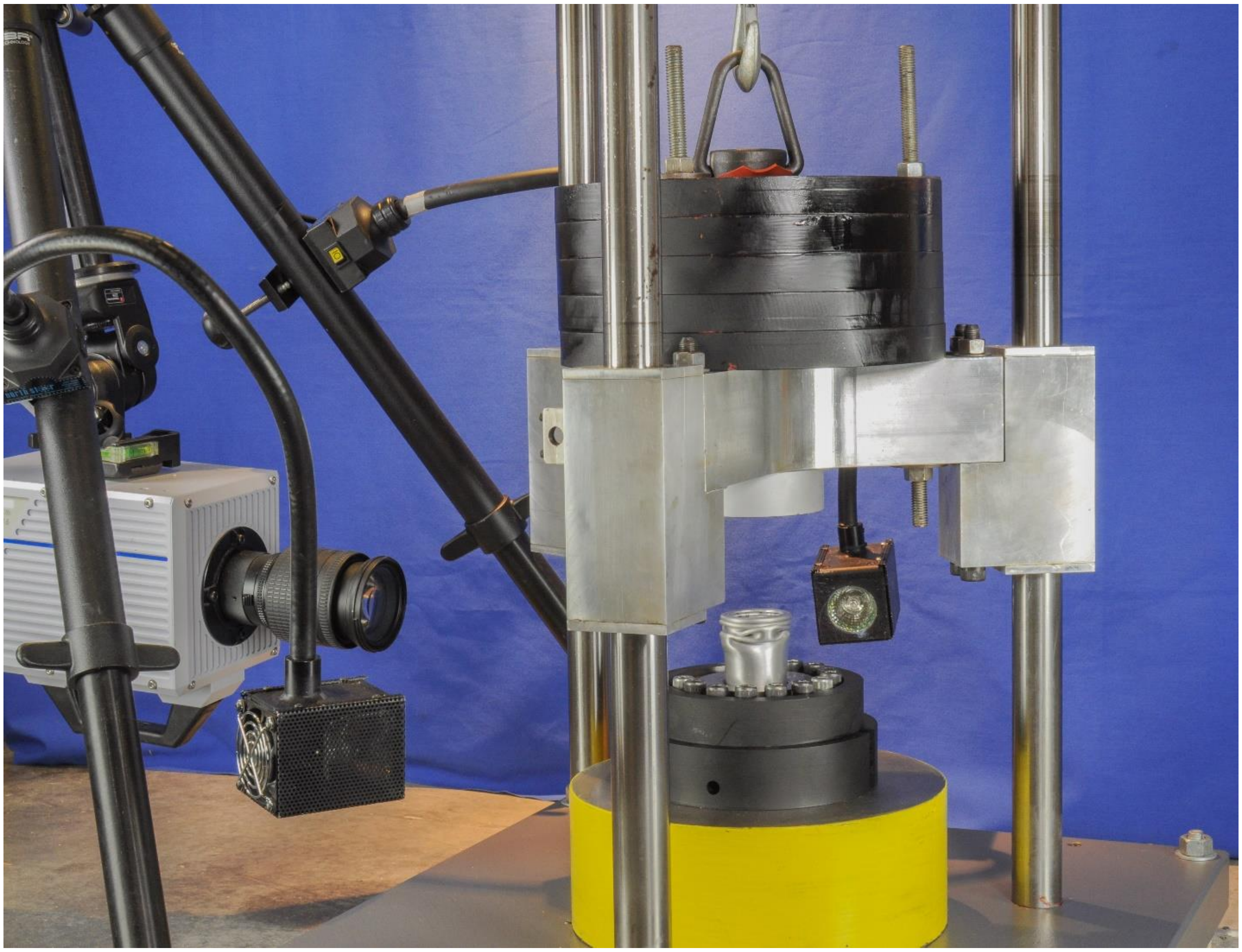

Fig. 2.6: Drop weight test facility for dynamic crushing experiments.

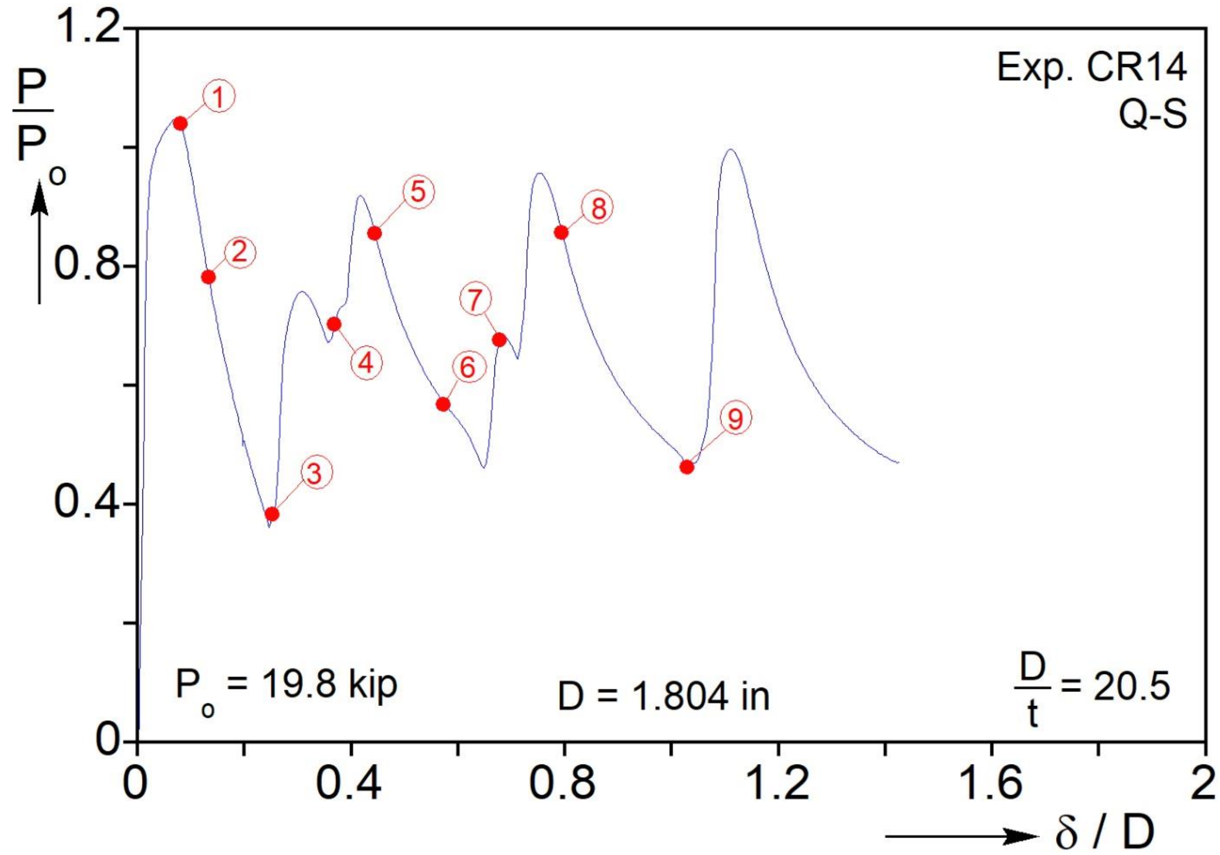

Fig. 2.7: Force-displacement quasi-static crushing response for a tube with D/t = 20.5.

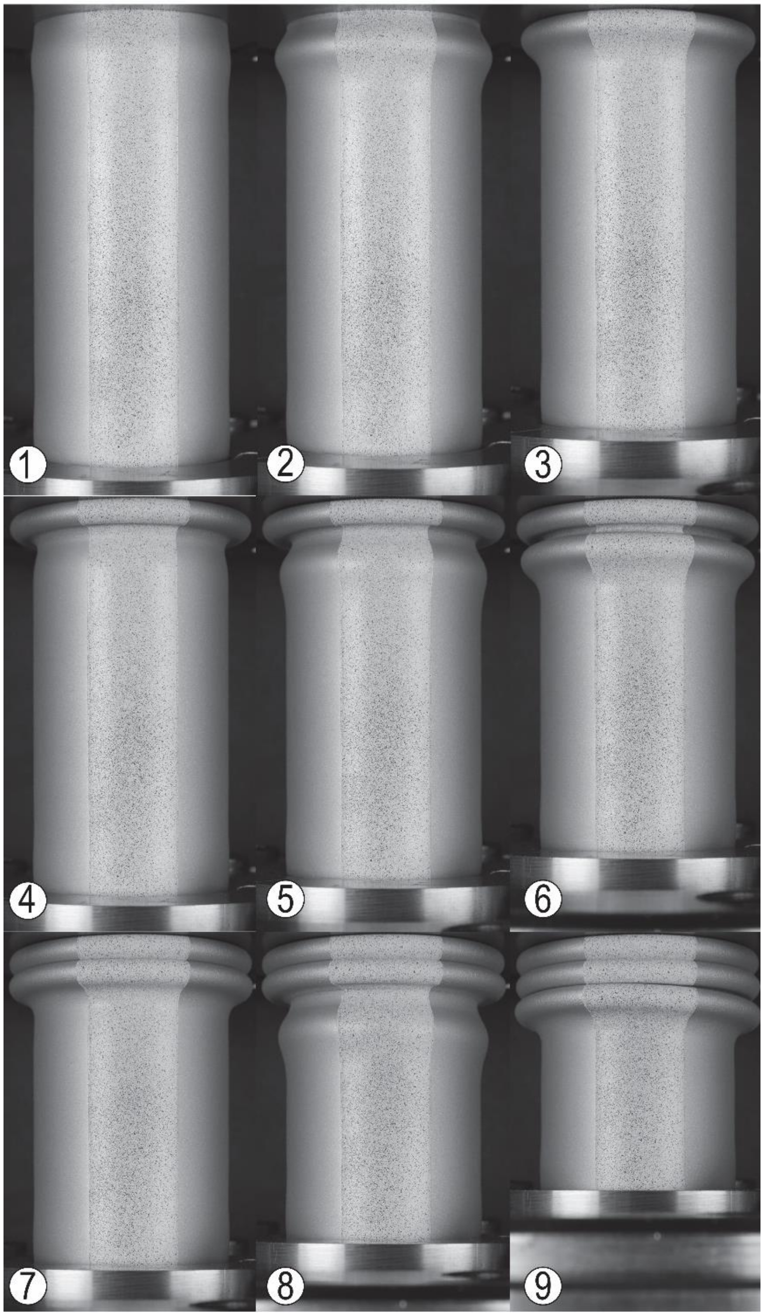

Fig. 2.8: Sequence of crushing configurations showing the evolution of axisymmetric folding corresponding to the numbered bullets on the response of CR14 in Fig. 2.7.

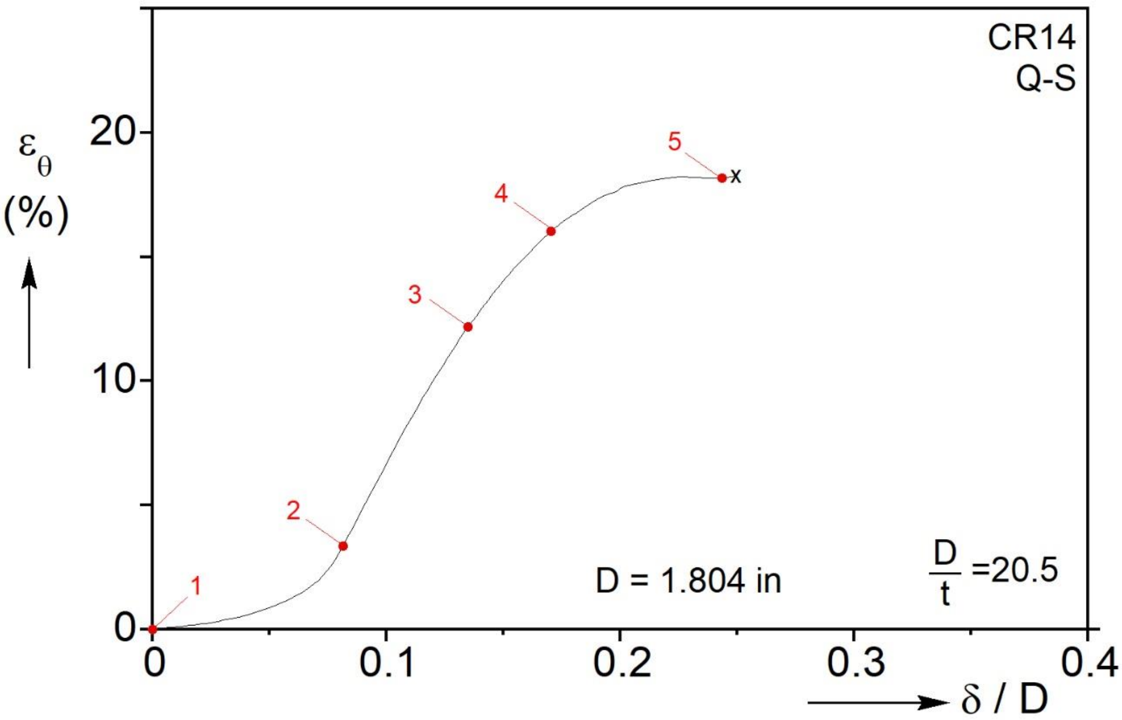

Fig. 2.9: Hoop strain-displacement quasi-static crushing response for a tube with D/t = 20.5.

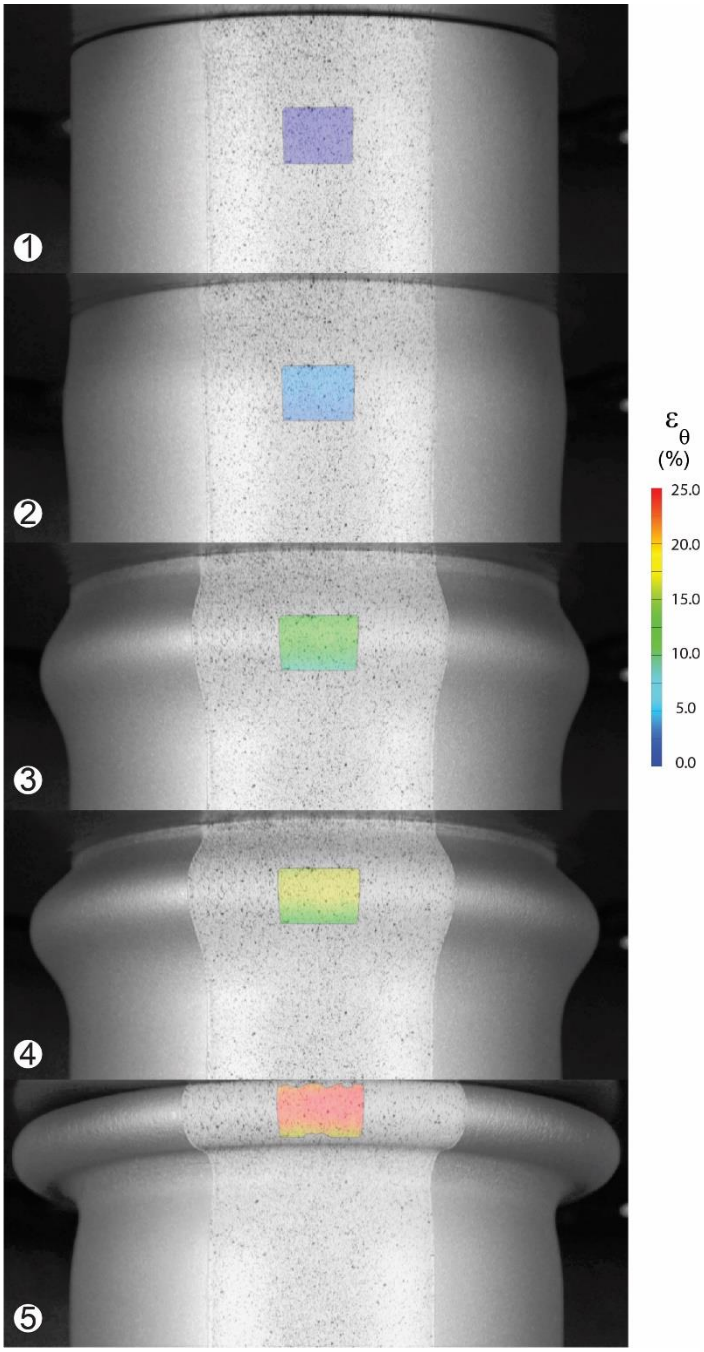

Fig. 2.10: Sequence of crushing configurations for quasi-static crushing experiment CR14 with in-plane hoop strain contour overlay corresponding to the numbered bullets of Fig. 2.9.

Fig. 2.11: Images of the specimen CR14 crushed. (a) Side view and (b) top view.

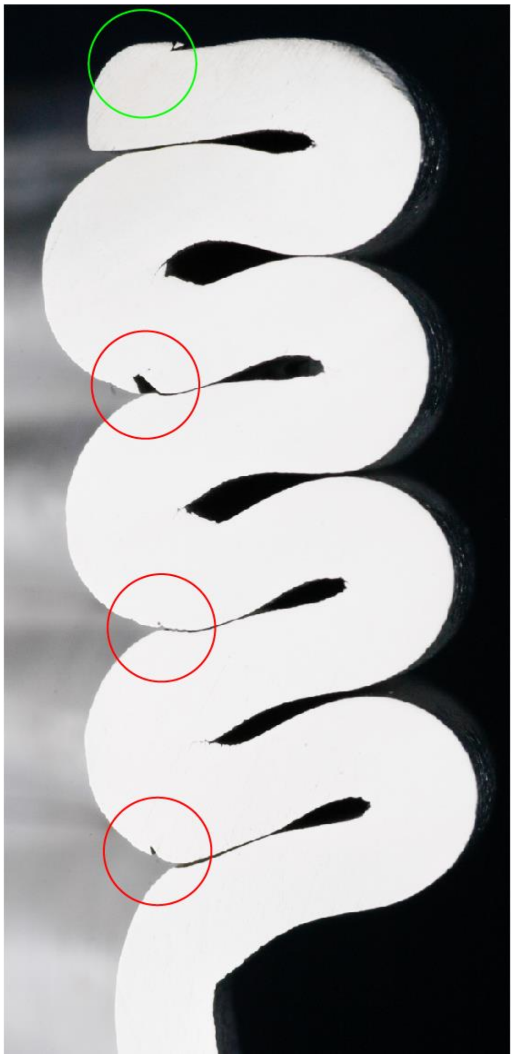

Fig. 2.12: Sectional view of the four axisymmetric folds that develop in specimen CR14. Observed failures in the red circled zones. Rounded top edge highlighted in green circle.

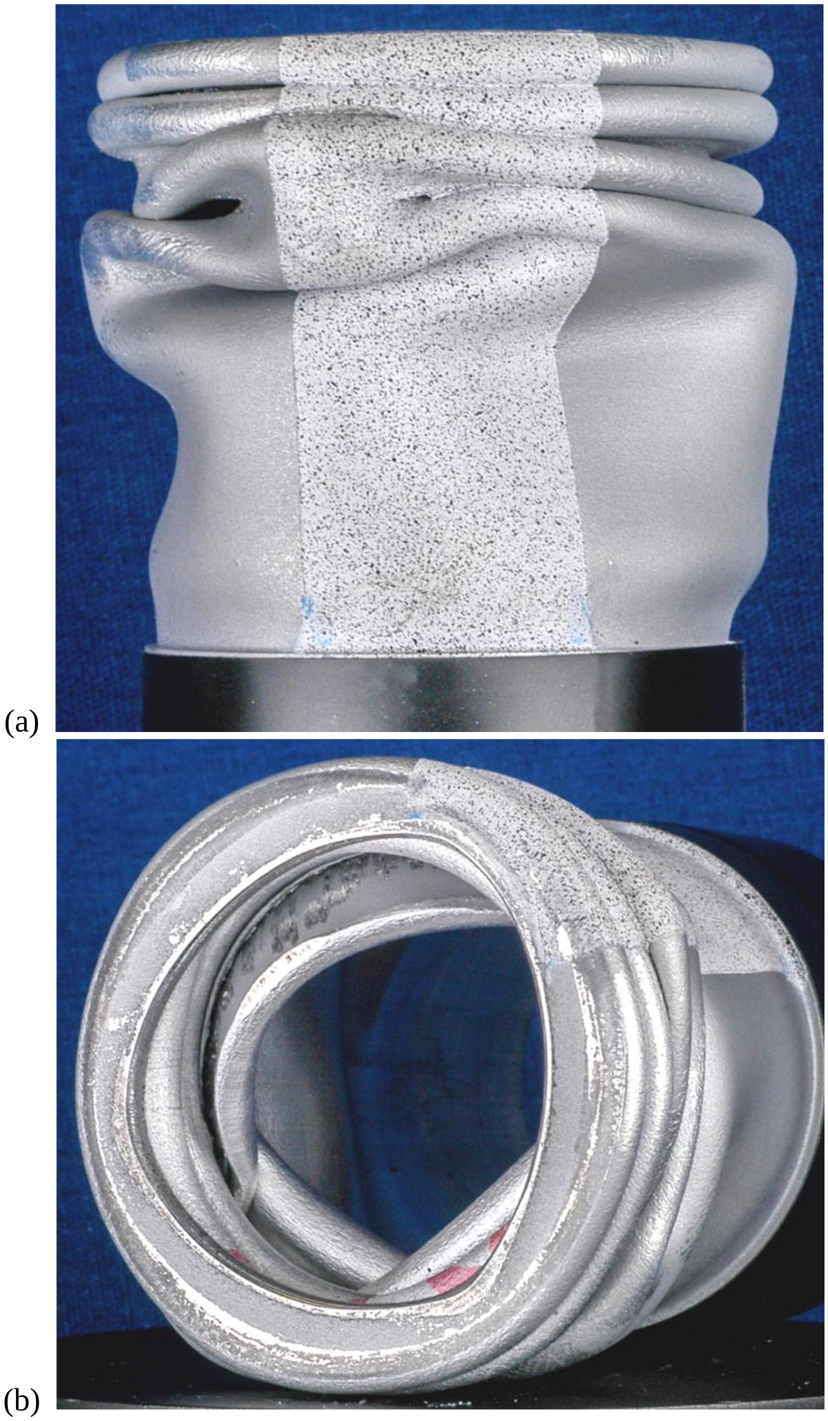

Fig. 2.13: Images of the specimen CR16 crushed. (a) Side view and (b) top view.

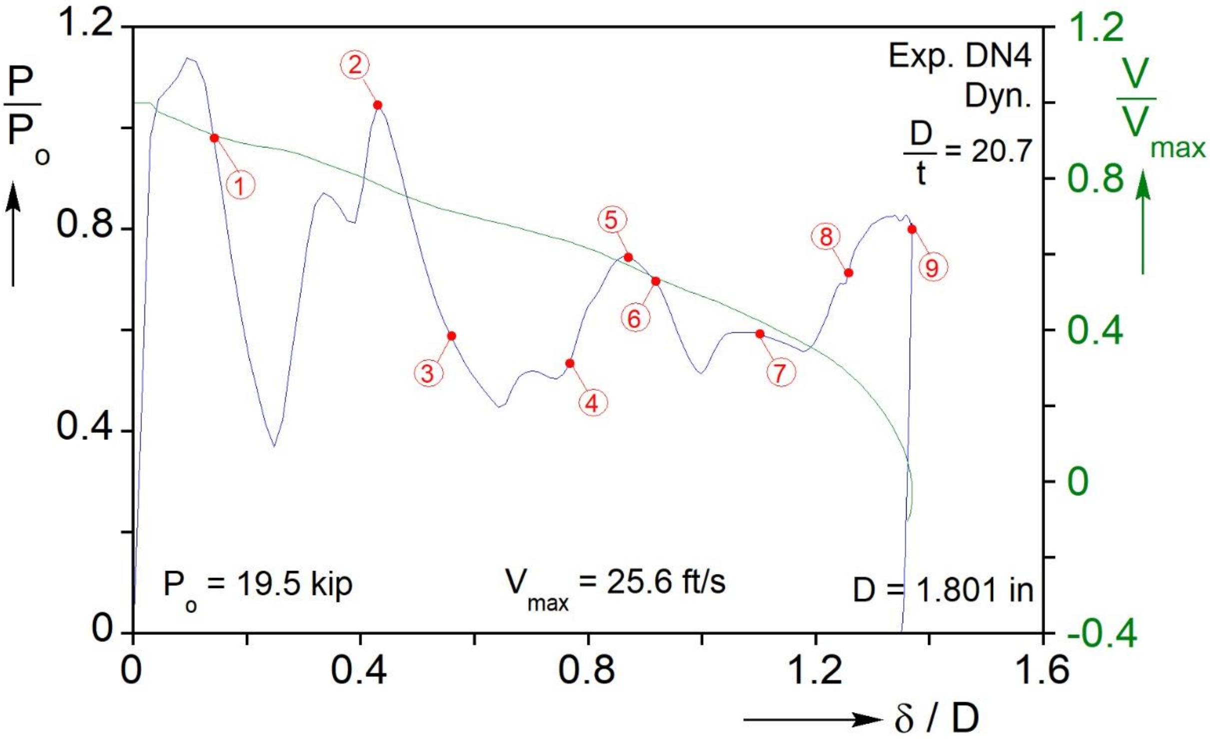

Fig. 2.14: Force- and velocity-displacement responses for a dynamic crushing experiment with D/t = 20.7.

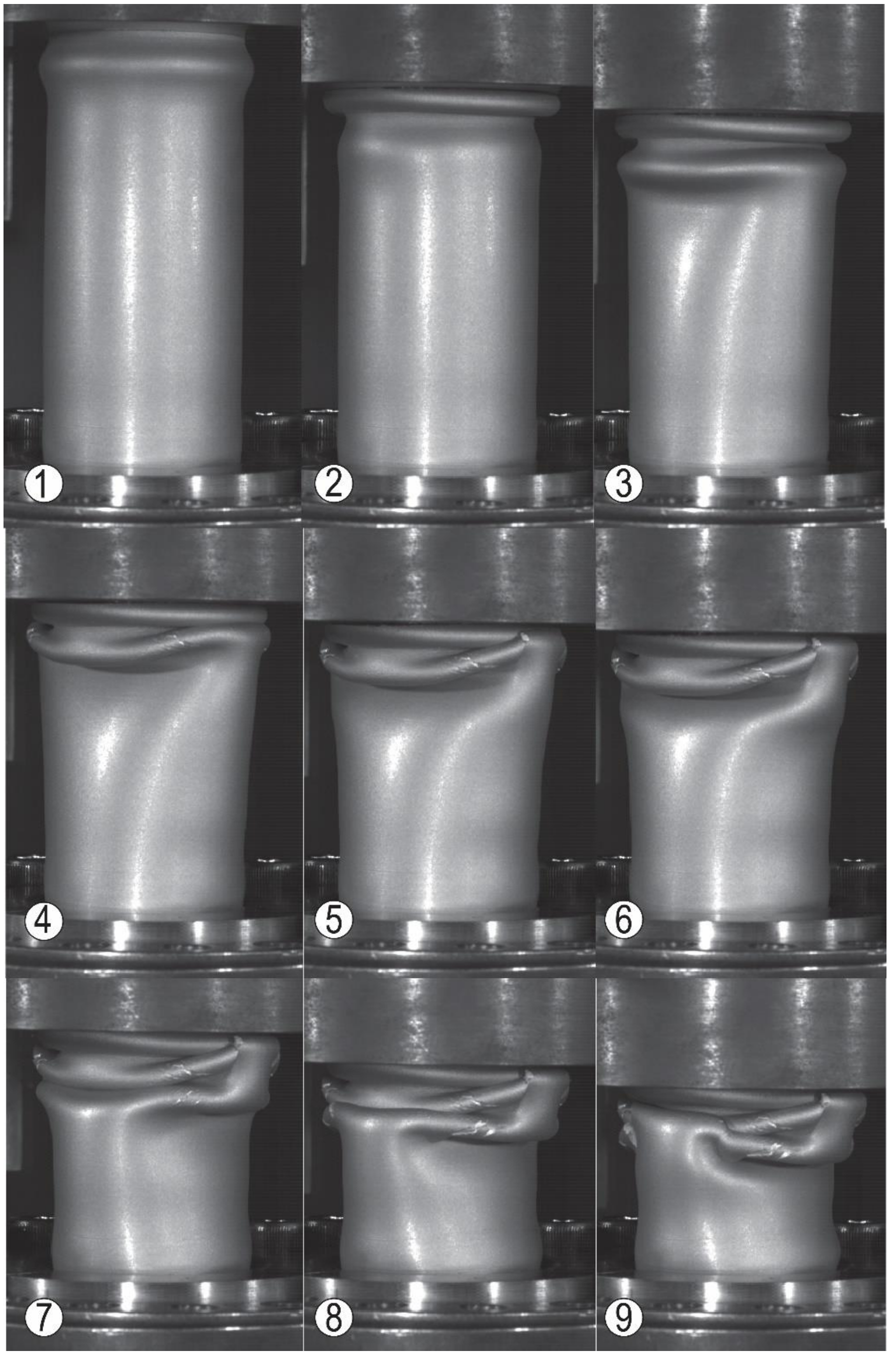

Fig. 2.15: Sequence of dynamic crushing configurations showing the evolution of mode switch and failure corresponding to the numbered bullets on the response of DN4 in Fig. 2.14.

Fig. 2.16: Image of the specimen DN4 crushed showing failure during mode switch.

Fig. 2.17: Photograph of specimen cross section from experiment DN4 showing the protrusions that has torn through the thickness.

Chapter 3: Constitutive Modeling

This work is concerned with the numerical simulation of the structural response and induced strains of Al-6061-T6 aluminum circular tubes under axial crushing. It has been well established that large deformation and forming processes can be heavily influenced by the adopted constitutive model, particularly in the prediction of the onset of failure (e.g., Giagmouris et al., 2010; Tardif and Kyriakides, 2012; Chen et al. 2019). This chapter outlines the Hosford (1972) non-quadratic yield function shown to be suitable for aluminum alloys, and the Barlat et al. (2005) anisotropic yield function that are used in subsequent crushing simulations. The von Mises yield function is also used in some simulations for completeness and comparison.

3.1 CHARACTERIZATION OF ISOTROPIC AND ANISOTROPIC YIELD FUNCTIONS

It is well recognized that plastic behavior of aluminum alloys is better represented by a non-quadratic yield function such as the one proposed by Hosford [1972]. This model written in terms of the principal stress deviators is given as:

$$F = [(|s_1 - s_2|^k + |s_2 - s_3|^k + |s_3 - s_1|^k)/2]^{1/k} \qquad (3.1)$$

where as is typical for FCC metals such as our Al-6061-T6, $k = 8$. Note that when $k = 2$, (3.1) reduces to the von Mises yield function.

Barlat et al. (2005) introduce anisotropy through the following yield function, hither to referred to as Yld04-3D:

$$\begin{aligned} F = [(&|S'_1 - S''_1|^k + |S'_1 - S''_2|^k + |S'_1 - S''_3|^k + |S'_2 - S''_1|^k + |S'_2 - S''_2|^k \\ &+ |S'_2 - S''_3|^k + |S'_3 - S''_1|^k + |S'_3 - S''_2|^k + |S'_3 - S''_3|^k])/4]^{1/k} \end{aligned} \qquad (3.2)$$

Anisotropy is introduced via two linear transformations of the Cauchy stress tensor $\boldsymbol{\sigma}$ to construct $\boldsymbol{S}'$, $\boldsymbol{S}''$. These transformations are obtained as follows:

$$\boldsymbol{S}' = \boldsymbol{C}'\boldsymbol{s} = \boldsymbol{C}'\boldsymbol{T}\boldsymbol{\sigma} = \boldsymbol{L}'\boldsymbol{\sigma} \qquad (3.3a)$$

and

$$\boldsymbol{S}'' = \boldsymbol{C}''\boldsymbol{s} = \boldsymbol{C}''\boldsymbol{T}\boldsymbol{\sigma} = \boldsymbol{L}''\boldsymbol{\sigma} \qquad (3.3b)$$

where $\boldsymbol{C}'$, $\boldsymbol{C}''$, $\boldsymbol{T}$, $\boldsymbol{L}'$, and $\boldsymbol{L}''$ are appropriate transformation tensors that introduce anisotropy. $\boldsymbol{T}$ is the standard linear transformation tensor of the Cauchy tensor $\boldsymbol{\sigma}$ to yield its deviator $\boldsymbol{s}$. $\boldsymbol{C}'$ and $\boldsymbol{C}''$ contain the 18 anisotropy parameters as follows:

$$C' = \begin{bmatrix} 0 & -c'_{12} & -c'_{13} & 0 & 0 & 0 \\ -c'_{21} & 0 & -c'_{23} & 0 & 0 & 0 \\ -c'_{31} & -c'_{32} & 0 & 0 & 0 & 0 \\ 0 & 0 & 0 & c'_{44} & 0 & 0 \\ 0 & 0 & 0 & 0 & c'_{55} & 0 \\ 0 & 0 & 0 & 0 & 0 & c'_{66} \end{bmatrix} \tag{3.4a}$$

and

$$C'' = \begin{bmatrix} 0 & -c''_{12} & -c''_{13} & 0 & 0 & 0 \\ -c''_{21} & 0 & -c''_{23} & 0 & 0 & 0 \\ -c''_{31} & -c''_{32} & 0 & 0 & 0 & 0 \\ 0 & 0 & 0 & c''_{44} & 0 & 0 \\ 0 & 0 & 0 & 0 & c''_{55} & 0 \\ 0 & 0 & 0 & 0 & 0 & c''_{66} \end{bmatrix} \tag{3.4b}$$

The principal values of $\boldsymbol{s}', \boldsymbol{s}''$, (S'_1, S'_2, S'_3) and (S''_1, S''_2, S''_3), respectively, are evaluated analytically.

The exponent k is again assigned the value of 8. When yielding is isotropic, all coefficients in (3.4a) and (3.4b) are equal to 1 and thus (3.2) reduces to Hosford's isotropic yield function in (3.1).

3.2 MATERIAL HARDENING AND CALIBRATION OF THE CONSTITUTIVE MODELS

The material stress-strain response is extracted from a uniaxial tension test which necks at a strain of about 8%. The stress-strain response of this Al-6061-T6 alloy was performed on a dogbone specimen and the response is given in Fig. 3.1. The limit load occurs at a strain of about 8% and is marked on the response.

It has been shown by many (e.g., Tardif and Kyriakides, 2012; Chen et al., 2018; Chen et al., 2019) that in addition to a properly calibrated non-quadratic yield function, a stress-strain response that captures material hardening to large enough strains is vital for accurate numerical modeling predictions. Chen et al. (2019) calibrated the Yld04-3D model using a series of 7 tension-torsion experiments, a simple shear test, a “plane strain” tension test, a uniaxial tension test on an axial strip, and 7 experiments of combined internal pressure and axial tension (see Appendix A of Chen et al., 2019). The constants determined are listed in Table 3.1.

The calibrated model was subsequently used to extract the material hardening response from a pure torsion experiment. The material hardening was also extracted using the von Mises (VM) and Hosford (H8) models. Fig. 3.2 shows the three hardening response extrapolated to strains of 120%. It must be mentioned that the yield stress of the actual tubes used in the crushing experiments was somewhat lower than the one of Chen et al. (2019). Thus, the responses shown in Fig. 3.2 where shifted downwards by a small amount to match this yield stress.

Table 3.1: Anisotropy parameters for Yld04-3D (Chen et al., 2019).

c'_{12}	c'_{13}	c'_{21}	c'_{23}	c'_{31}	c'_{32}	c'_{44}	c'_{55}	c'_{66}
1.028	1.150	1.162	.941	0.679	0.985	1.0	1.0	1.367
c''_{12}	c''_{13}	c''_{21}	c''_{23}	c''_{31}	c''_{32}	c''_{44}	c''_{55}	c''_{66}
0.713	0.683	0.847	1.093	1.056	0.962	1.0	1.0	0.695

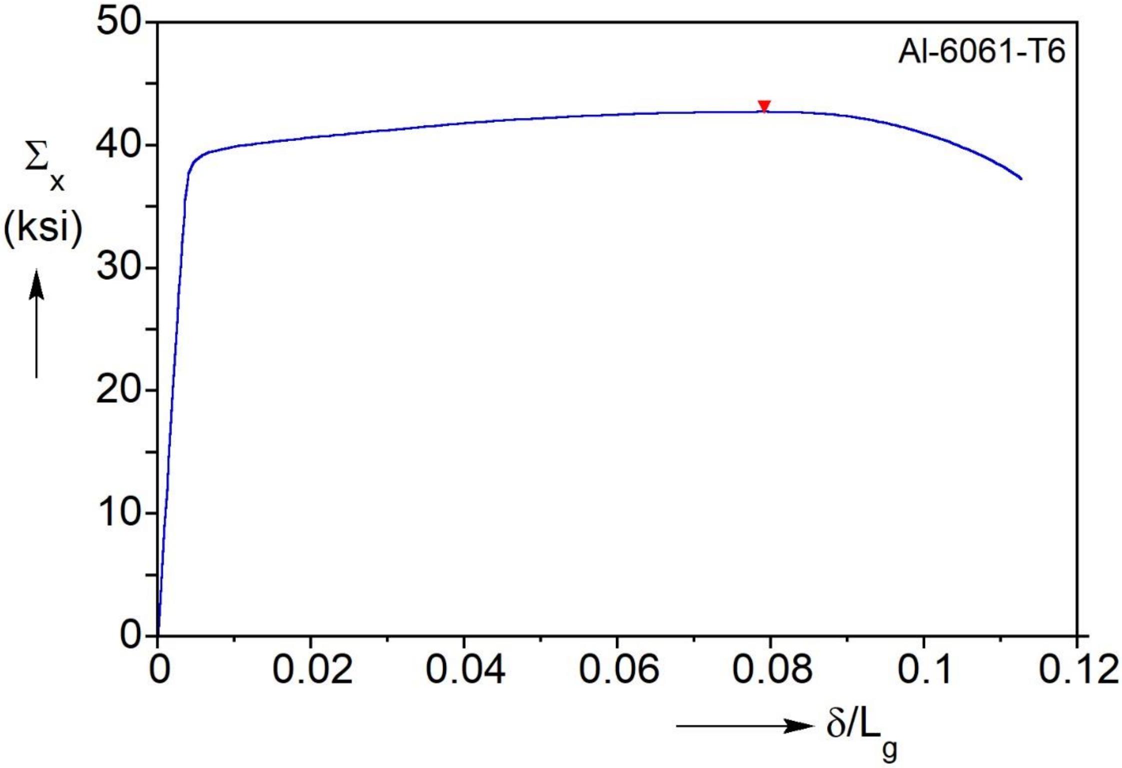

Fig. 3.1: Nominal uniaxial stress-strain response of Al-6061-T6.

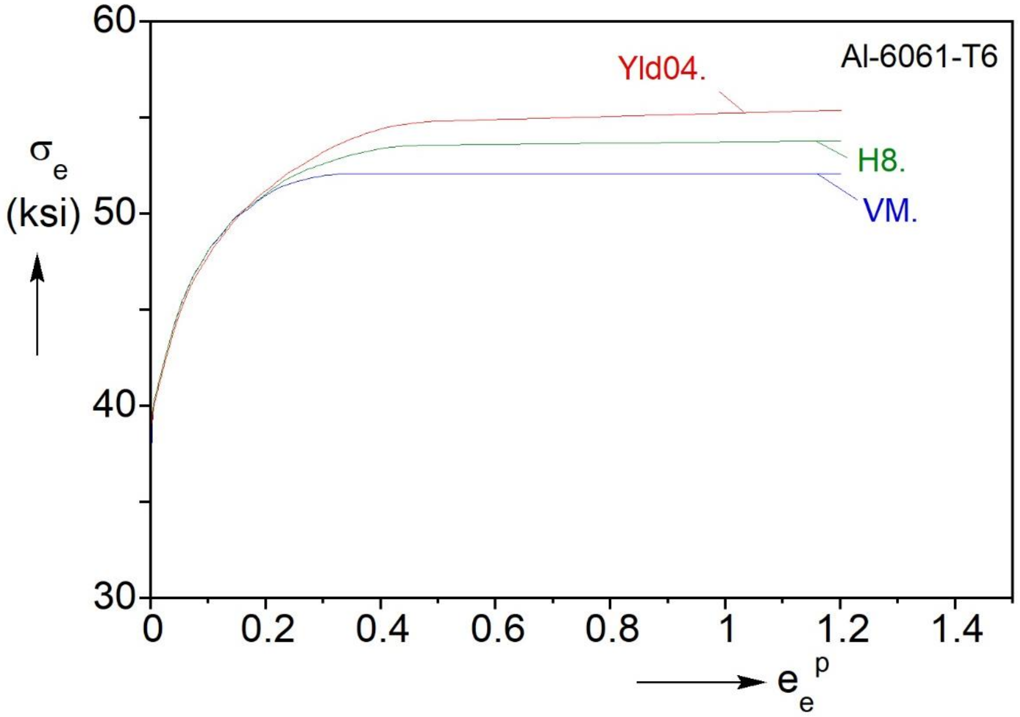

Fig. 3.2: Extracted true stress-plastic strain curves for the three constitutive models.

Chapter 4: Analysis

This Chapter uses suitably nonlinear finite element models to simulate the tube crushing experiments presented in Chapter 2. The finite element model is developed using LS-Dyna R11.0 Explicit Finite Element code. This code was chosen due to its ability to handle the non-linearity of large deformation and contact that are fundamental to the tube crushing problem. Being an explicit code also helps overcome thorny convergence problems that periodically arise. Three constitutive models are considered in the simulations: the von Mises, non-quadratic Hosford, and the anisotropic Yld04-3D model of Barlat et al. (2005). LS-Dyna R11.0 features the Yld04-3D as a built-in material model. The goals of the modeling efforts were to reproduce the structural response (P-δ), to study the effect of the adopted constitutive model on the solution, and on the strains at the points where failure occurred in the experiments. Both the quasi-static and dynamic crushing experiments are simulated.

4.1 MESHING AND MODEL CONSTRUCTION

4.1.1 Quasi-Static Model

The geometry definition of the 3-D model is shown in Fig. 4.1a. The values of D, t, and L measured in the experiments were used to build the 3-D geometry in Abaqus' pre-processor software. The thickness eccentricity was included in the geometry by shifting the inner surface of the tube off of the center in the $r-\theta$ plane by $\Xi_o t$ (see Fig. 4.11 in Kyriakides and Corona, 2007).

The 3-D geometry was meshed using fully integrated S/R 8-noded solid elements arranged in a medial axis pattern about the center of the tube in the axial direction. A section of the mesh is shown in Fig. 4.1b where N_t, N_θ, and N_L are the number of elements in the radial (thickness), circumferential, and axial direction, respectively. A Python routine was used to convert the Abaqus mesh input file to one that is compatible with LS-Dyna.

A convergence study was conducted using 2-D axisymmetric shell elements and it was determined that 6 elements through the thickness were sufficient to predict the structural response of an axisymmetric folding experiment. The values of N_θ and N_L were subsequently chosen such that the elements of the mesh had a nearly 1:1:1 aspect ratio. Thus, for example the mesh of CR14 tube simulation consisted of approximately 288,000 elements. This large number of elements necessitated the use of massively parallel processing (MPP) computation using Lonestar5 supercomputer at the Texas Advanced Computing Center (TACC).

The model was simplified by removing the lower grip shown in Fig. 2.2. The specimen was thus crushed between two analytical rigid surfaces. One of the surfaces was fixed in space and the tube was crushed by prescribing a displacement to the second. An automatic surface-to-node contact algorithm was assigned by defining all nodes of the tube as slave nodes in the rigid wall card. This contact algorithm checks for penetration of integration points through the analytical rigid surface. Automatic single-surface self-contact was assigned to the tube. This algorithm checks for penetration of integration points into the tube surface. A Coulomb friction coefficient of $\mu = 0.35$ was assigned to all contact definitions. These contact algorithms are compatible with MPP per the LS-Dyna Keyword Manual: Volume I.

Mass scaling was utilized in the explicit code to reasonably expedite the calculation. The scaling was done manually via parametric study of mass and time effect on the calculation. Suitable values for the scaled mass were established such that the kinetic energy of the system remained several orders of magnitudes lower than the internal energy of system. Furthermore, it is confirmed that contact and sliding did not produce any significant instabilities in the energy or the structural responses.

4.1.2 Dynamic Model

The dynamic model used the full tube specimen geometry, including the grip. The test section was meshed with the same scheme as the quasi-static model. The grip section was meshed with a similar, but coarser, mesh as the test section. The meshed tube geometry is shown in Fig. 4.2a. The 3-D geometry of the ID plug, spacer, and impactor were constructed in Solidworks CAD. They were meshed in Abaqus with fully integrated 8-noded solid elements using the same medial axis scheme as the tube. Again, all mesh data was converted from Abaqus to LS-Dyna input format.

A schematic of the complete dynamic model is shown in Fig. 4.2b. The ID plug, spacers, and tube were assembled very closely together but were not in contact. The bottom nodes of the ID plug, spacer, and tube were constrained against translation and rotation in all directions. The impactor was placed just above the tube and constrained to only vertical translation. The ID plug, spacer, and impactor were assigned rigid material properties. Automatic surface-to-surface contact was defined between the rigid parts and the tube. The rigid parts were assigned as the master and the tube was designated as the slave. A soft contact definition was used for this surface-to-surface contact algorithm in order to reduce contact instabilities during impact. The algorithm only considers additional penetration past the first penetration as contributing to a force as shown in Fig. 4.3. It determines the stiffness of the contact force from additional penetration automatically based on the time step. It was found that this 'soft' contact algorithm does not affect the global structural response. The same automatic, single-surface, self-contact as the quasi-static model was assigned to the tube and the default 'hard' contact algorithm was retained.

As mentioned in Chapter 2, none of the dynamic experiments collapsed fully in an axisymmetric fashion. Instead, the crushing switched to either mode-2 or mode-3 following some initial axisymmetric folding. The mode switch was suspected to be due to misalignment of the impactor. Early dynamic numerical simulation results suggested that the switching was not due to inertial effects. This led to a study of the effect of small misalignment between the impactor and the top surface of the tube on the mode switch. This misalignment was introduced by rotating the impactor by a small angle as shown in Fig. 4.2b. The introduction of misalignment was accompanied by a reduction in the friction coefficient. For example, in the case of DN4, a friction coefficient of $\mu = 0.05$ and a misalignment of 0.4° reproduced the switch to a mode-2 fold after one axisymmetric fold as was the case in the experiment.

Mass scaling was also utilized in the dynamic experiments to expedite calculations. The impactor mass was assigned the mass of the experimental drop weight assembly and then scaled (increased) using the same scaling factor as the tube mass. The initial velocity for the impactor, V_i, was evaluated by matching the kinetic energy of the drop weight assembly to that of the impactor in the model. To ensure valid results from mass scaling, the predicted kinetic energy of the tube was confirmed to be much smaller than the internal energy of the tube. The structural responses were also checked for instabilities. A few simulations were calculated using the actual mass and time conditions and it was found that the kinetic energy of the tube is also predicted to be much lower than the internal energy.

4.2 ANALYSIS RESULTS

4.2.1 Quasi-Static Analysis Results

This section will present the simulation of axisymmetric, quasi-static crushing of experiment CR14. The predicted P-δ responses, normalized by the yield load P_o and the tube diameter D, calculated using the VM, H8, and Yld04-3D models are shown in Figs. 4.4, 4.5, and 4.6, respectively. Each simulated crushing response is compared to the experimental response. The force-displacement response from each model features the same general pattern as the experimental response; the initial load maximum is followed by lower two-peak cycles. The smaller load peak gets smaller with each cycle ending up with a single peak at the end of the response. In the case of the VM model, the initial load maximum is higher than the experimental value. Corresponding results for the H8 and Yld04-3D models are very close to the measured initial load maximum. Following the initial load maximum, the VM P-δ response starts lagging behind the experimental one. The experimental response finishes its third cycle near δ/D = 1.05. By the end of the third loading cycle near δ/D = 1.24 (Fig. 4.4), the response is approximately half a loading cycle wavelength behind the experimental response. Now compare the H8 and Yld04-3D to the experiment. The first and second load cycles of both H8 and Yld04-3D follow the experimental response closely. Subsequently, the calculated force reproduces experimental value quite well but the displacement starts to slowly lag and to progressively accumulate for both models. The H8 model prediction (Fig. 4.5) finishes its third load cycle near δ/D = 1.20. The Yld04-3D response (Fig. 4.6) finishes the cycle near δ/D = 1.17. In the present study, the stress-strain curves used in the simulations originated from Scales (2019). The measured stress-strain data finished at a strain of just under 40%. Beyond this point, the three response were extrapolated as perfectly plastic (see Fig. 3.2). Bardi et al. (2003), who used VM plasticity, found that increasing/decreasing the slope of the extrapolated stress-strain response respectively increased/decreased the period of the cycles but had minor effect on the mean crushing load. Thus, we suspect that the perfectly plastic extrapolation plays a role in the observed differences in the period of the crushing cycle between the experimental and predicted responses.

Another contributor to the observed lagging in the calculated response is seen in the prediction of the hoop strain during the formation of the first fold. Fig. 4.7 compares the measured and calculated hoop strain in this part of the loading. Whereas H8 and Yld04-3D following the measured strain quite accurately, the VM model is significantly different. This difference contributes to the lag observed in the initial P-δ load

The P-δ response from the Yld04-3D simulation is shown in Fig. 4.8 and a set of corresponding crushing configurations in Fig. 4.9. The marked points are taken at similar locations along the response as in experiment CR14 (see Figs. 2.7, 2.8). The crushing configurations in Fig. 4.9 are sectioned in half to reveal the evolution of the axisymmetric folds that develop during the crushing. The simulation reproduces the inward sliding and rounding of the top tube surface. Images ②-④ show a view of this action that is difficult to observe during the experiment (see the green circled area in Fig. 2.12). The explicit formulation used in the models enabled the sliding to take place; it was an issue that was difficult to produce in Abaqus Standard/Implicit. The cross-section view in Fig. 4.9 provide also an additional perspective of the progressive loss of the first peak of the two-peak load cycles. Between images ⑥ and ⑦, the outside surface of the second fold makes contact with the first fold and the structure locally stiffens. This can be easily seen in the experiment in Figs. 2.7, 2.8. Near ⑦, the load reaches the first peak, drops briefly, and then the inside surfaces make contact. The response rises, reaches its second maximum, and the third fold begins to form as seen in ⑧. It is observed that as crushing progresses the inner and outer surfaces begin to make contact simultaneously, which erases the first load peak of the cycle. Such behavior was also observed experimentally and numerically in Bardi et al. (2003).

The strains developed during this crushing response are now examined in some detail. Fig. 4.10 shows again the force-displacement response but now featuring a set of eight equally spaced stations covering the second and third folds marked with numbered bullets. Axisymmetric cross-sections corresponding to these stations with superimposed equivalent plastic strain contours are displayed in Fig. 4.11. Marked on the deformed cross sections are five locations along the length labeled a-e, which represent sites where maximum strain is expected to develop. Each site is marked with a unique symbol for clearer identification in subsequent plots. Note that for clarity, images ①-④ are truncated just below c, whereas images ⑤-⑧ display more of the tube.

Figs. 4.12 and 4.13 show the equivalent plastic strain predictions for the inner and outer surface elements, respectively, plotted along the undeformed length of the tube x/L measured from the top of the tube. Included in each figure are the strain profiles along the length corresponding to each of the eight stations in Figs. 4.10, 4.11. We consider first the evolution of strain at site a in Fig. 4.12. From stations ① to ④, the strain in the neighborhood of a rapidly increases, reaching a level of about 68%. Subsequently, the strain remains constant as deformation has ceased in this neighborhood. It is important to note that site a is on an extrados and consequently the strain is mainly tensile. The strain at site b starts growing as the second fold starts to develop around station ①. The strain continues to grow in this vicinity until station ⑤ at which point the deformation ceases in this area. It reaches a maximum level of about 138%, however, since this site is on a fold intrados the strain is mainly compressive. Location c has a similar tensile strain trajectory as location a but develops later in the crushing history between stations ④-⑧. This site reaches maximum equivalent plastic strain of nearly 65%.

The evolution of strain at points on the outer surface elements is presented in Fig. 4.13. The strain concentration near $x/L = 0.25$ is nearly identical to the trajectory at b and thus is not elaborated on. Site d steadily rises between stations ③ and ⑧ and ceases to deform once it reaches a maximum strain of about 127%. After station ④, the strain in the neighborhood of site e starts to grow reaching a maximum value of 63%.

Sites a and c are located on extrados on inner folds where tensile failure is typically observed experimentally as highlighted in Fig. 2.12. On the other hand, an extrados of an outer fold, such as site e, does not show visible tensile failure in the experiment. The maximum values of strain reached in all these extrados locations are around 65%. Interestingly, the primary difference between a and c when compared to location e is the difference in tensile strain paths. Site c has almost twice the magnitude of tensile strain in the local axial frame when compared to site e. Bardi et al. (2003) observed that deformed thickness and radius of the inside folds is larger than the outside folds and thus take more space in the axial direction. This difference was noticed to result in a progressively increase in the inclination of the outer folds. A similar inclination can be seen in the third fold of station ⑧ in Fig. 4.11. In addition, Bardi et al. found that the deformed thickness of the inner fold was larger than the outer fold. These differences in deformed fold geometry are consistent with the present results. This difference results in larger local tensile strains on the inner fold extradoses and is responsible for the failures observed in the experiments to occur at these sites.

It worth comparing the effect of the constitutive model adopted on such equivalent plastic strain profiles. Fig. 4.14 plots strain profiles predicted for the inner surface elements using the three constitutive models adopted. Sites a, b, and c are marked on the Yld04-3D strain profile for reference regarding the discussions around Figs. 4.10-13.

As mentioned previously, the crushing load-displacement cycles predicted by the three constitutive models are somewhat out of phase. For example, the third load valley, which corresponds to a crushed state just before image ⑧, occurs at δ/D of 1.17 for Yld04-3D, 1.20 for H8, and 1.24 for VM. Thus, in Fig. 4.14 the third load valley of each response was chosen as the configuration to compare the strain profiles. In general, the peaks of all model predictions are quite similar. However, the models vary slightly in locations such as the points on the intrados near $x/L = 0.35$ or the extrados point near $x/L = 0.5$. Here, the Yld04-3D and H8 models predict slightly lower peaks than the VM. The main difference between the models is the prediction of where the folds form on the undeformed location x/L.

4.2.2 Dynamic Analysis Results

This section presents the results of the dynamic simulation of experiment DN4. The predicted force-displacement response using the Yld04-3D constitutive model is shown in Fig. 4.15. Included is the evolution of the velocity of the impactor. The calculated P-δ response under predicts the initial peak load somewhat whereas the following load drop is predicted accurately. The two load-peak axisymmetric cycle that follows is reproduced well but the two load peaks are again under predicted. The response of the mode-2 cycle is captured but with some delay. Beyond this point, the two sets of results differ because of the failure that occurred in the experiment. The predicted impactor velocity follows the measured impactor velocity very well. The velocity decreases nearly linear and drops off rapidly towards the end of the crushing event. The two responses only deviate near the end of the respective cycles.

Marked on the predicted response are nine stations which correspond to the crushing configurations included in Fig. 4.16. An effort was made to place the stations at locations similar to those marked on the experimental response (see Fig. 2.14). The two-peak axisymmetric crushing cycle is nearing completion at ②. Image ③ shows the first signs of a switch to a mode-2 folding pattern as was the case in the experiment (see Fig. 2.15). From ④ on, the mode-2 folding becomes clearer and the force-displacement exhibits a lower, single peak cycle that reaches its maximum at ⑤ and ends just before ⑦. A second mode-2 cycle initiates but at ⑨ the kinetic energy of the impactor is depleted and the structure unloads elastically.

As mentioned previously, the mode switch was produced by introducing a misalignment to the impactor and simultaneously reducing the contact friction coefficient. Fig. 4.17 compares this force-displacement response with one from a simulation in which misalignment was not included, and a higher friction coefficient was used. In the latter case, the tube crushes in a fully axisymmetric fashion. The force-displacement response features the typical two-peak behavior and progressively reduces to a single peak. The difference in magnitude of the first two-peak load cycle near $\delta/D = 0.4$ may suggest that some asymmetry has set in the first load cycle.

Dynamic P-δ responses were produced using the three constitutive models discussed earlier. The three responses calculated are compared to the experimental one in Fig. 4.18. All three calculated responses trace similar trajectories and thus the VM and H8 results exhibit similar differences from the experiments as those of the Yld04-3D model outlined above. The calculated responses slightly under predict the initial peak load with the VM model having a somewhat higher peak load than the other two. The two load-peak axisymmetric cycle of the experiment are higher than those predicted by the three models. The ‘lag’ of the structural response of the VM model, mentioned in Section 4.2.1, can be seen again starting with the first load valley.

In concert with the experiment, after the two-peak response, the three models predict a switch to mode-2 folding. The first mode-2 cycle begins at the valley near $\delta/D = 0.7$. The arrows on the responses mark the location where the first mode-2 folding cycle ends for each case. The Yld04-3D, H8, and VM models predict the end of the cycle at $\delta/D = 1.10$, 1.14, and 1.23, respectively. All three fall quite short of the experimental results in which the cycle ends at $\delta/D = 1.0$. The early end of the cycle observed experimentally is suspected to be due to the tearing failure that occurred. The tearing reduced the local energy absorbed and enabled the formation a second mode-2 fold.

Interestingly, at the end of the mode-2 cycle, the VM predicts the structure has absorbed nearly all the available kinetic energy and unloads. In the case of the Yld04-3D and H8 simulations a second mode-2 fold starts to form but the folding is interrupted before a new load peak is reached.

The predicted strains of the Yld04-3D model are now presented in a similar fashion as in the quasi-static results in Section 4.2.1. Section 2.3.2 discussed the protrusion that tears away during the mode switch (see Figs. 2.15-2.17). Fig. 4.19 shows the same Yld04-3D response with stations ①-⑧ marked during the period that the failure developed in the experiment. Fig. 4.20a shows the tube in a crushed state with a red line marking the location where the sections shown Fig. 4.20b are taken. Superimposed on the crushed sections are equivalent plastic strain contours. The strain on the inner surface of the model is plotted along the undeformed length of the tube in Fig. 4.21. Included are strain profiles for each of the eight stations marked in Fig. 4.19. Site a marked in Fig. 4.20b is seen to develop the highest strain during this part of the response. The strain grows steadily from stations ①-④ when it starts rising precipitously reaching a final value of about 192% at station ⑧.

Similar strain profiles are plotted for the outer surface in Fig. 4.22. Site b, marked on the sectioned configurations in Fig. 4.20b, is nearly across the thickness from site a. The strain at b grows slowly from stations ①-④, but picks up in subsequent stations, and reached a maximum value of about 67%.

The following observations can be made from the DN4 results presented:

- The maximum equivalent plastic strains on the tube axial section analyzed occur at points a and b with the value at a reaching a level just under 200%. The section chosen approximately matches the section where one side of the tear occurred in the experiment. Fig. 4.23a shows the tube from the experiment cut along a diagonal that passed through the midpoints of the tears. Fig. 4.23b shows the model sectioned along the same plane (see green in in Fig. 4.20a). The vertical red lines correspond to the locations of maximum strain on this section–inside surface. They correspond to the through thickness tears in the experimental image. (Note that these locations do not correspond to point a but are quite close to it.)

- It is clear from Figs. 4.19-4.22 that very high strains develop first on the inner surface. This suggests that in the experiment failure probably began on the inside surface and propagated through the wall thickness. This, of course, can only be confirmed by adopting an appropriate failure criterion and tracking failure with a method such as element deletion, which is beyond the scope of this study.
- In the absence of failure, the model tube requires more energy for further crushing of the second mode-2 fold. However, by station ⑧ the available kinetic energy has been depleted, which causes the recorded force to decay also. By contrast, the torn tube in the experiment develops one more load peak. This again should be confirmed with a model that tracks the failure.

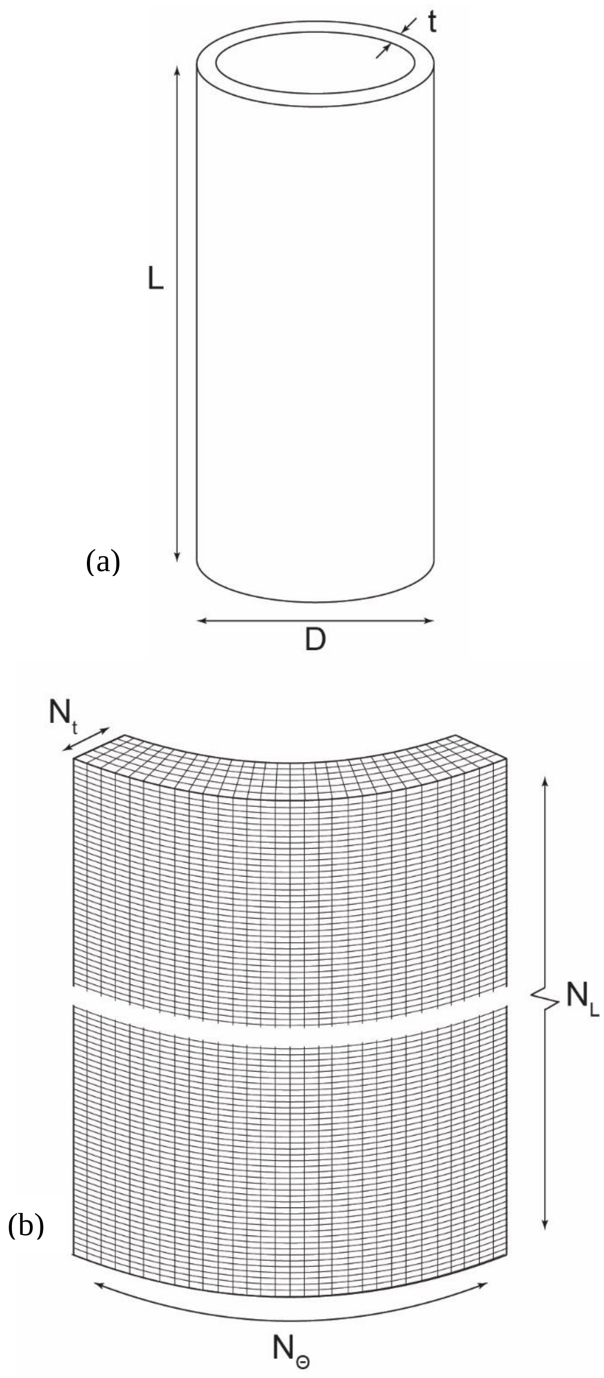

Fig. 4.1: (a) Quasi-static model tube geometry and (b) three dimensional finite element mesh of models.

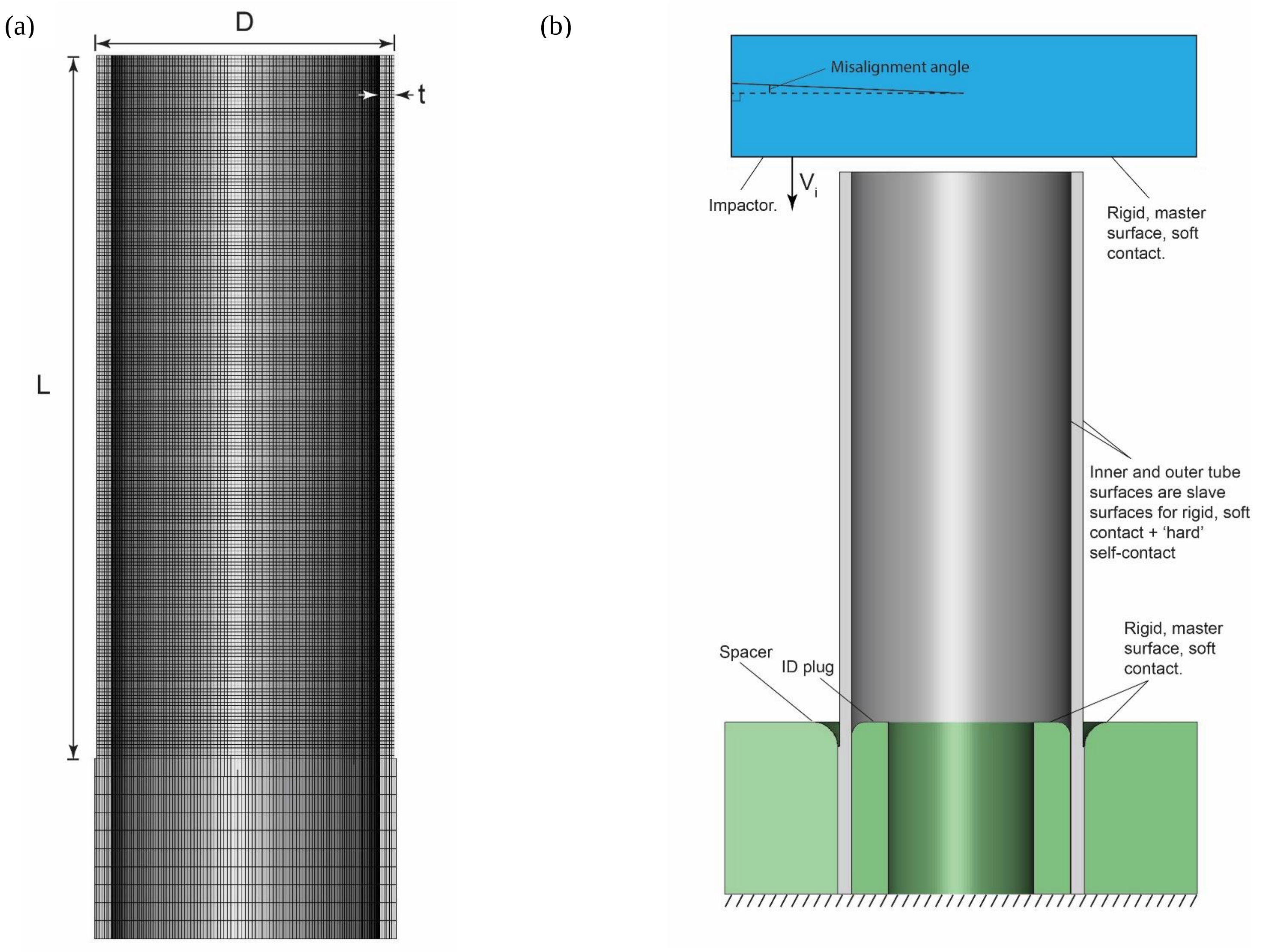

Fig. 4.2: (a) Cross-section of test section and grip section with mesh superimposed (b) Dynamic model schematic.

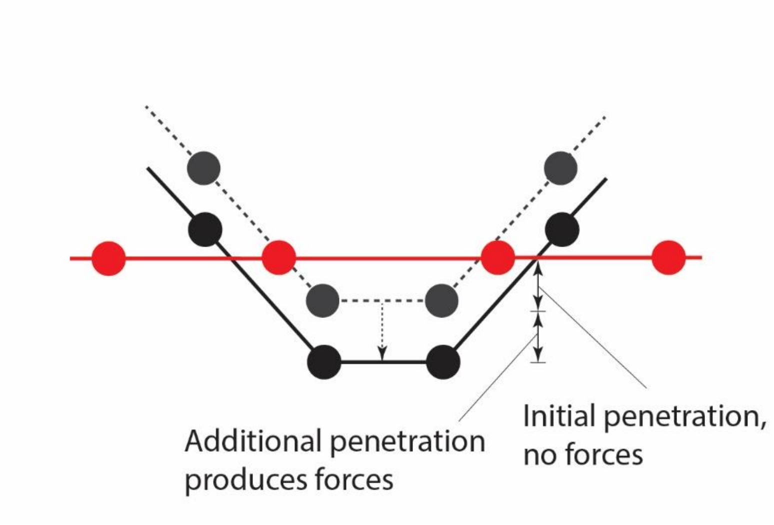

Fig. 4.3: Description of soft contact algorithm used in dynamic simulations showing that contact forces only arise after additional penetration past the initial value.

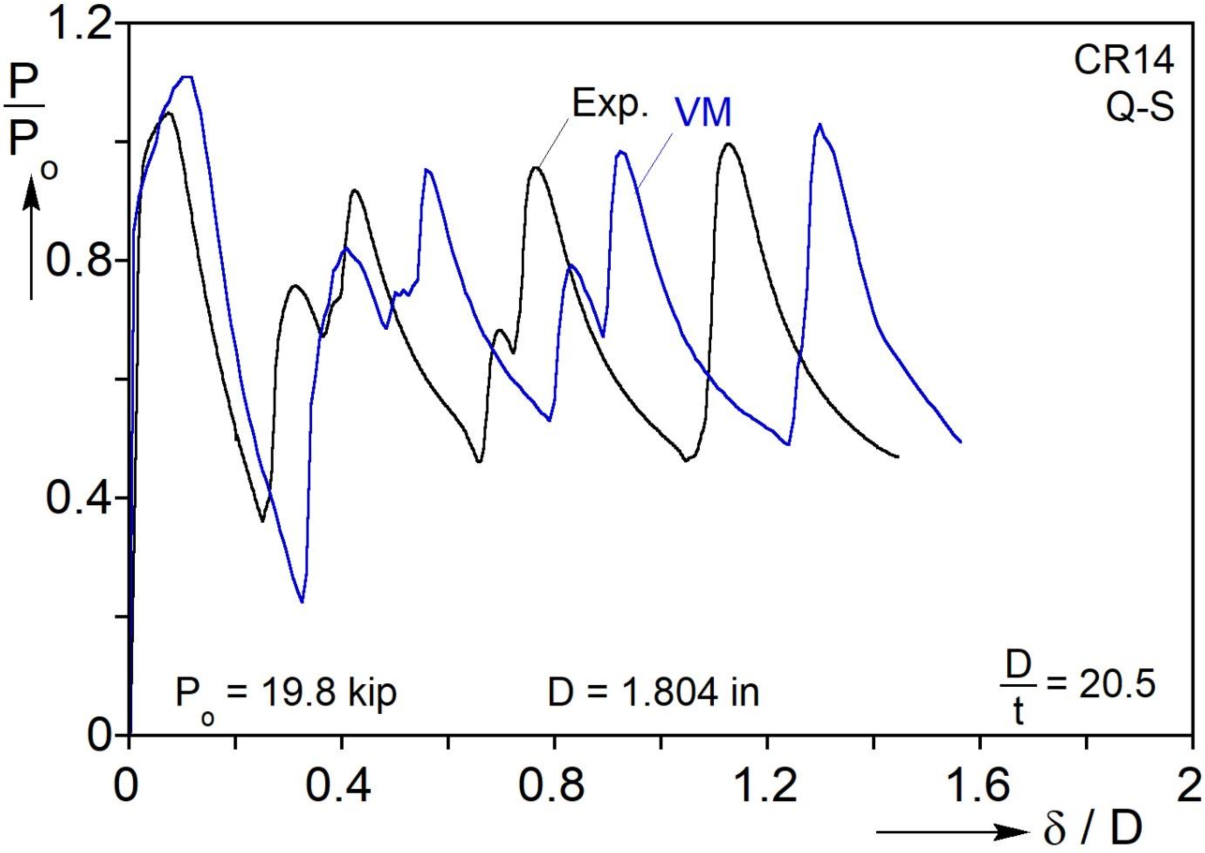

Fig. 4.4: Force-displacement crushing response of experiment and simulation of CR14 using VM model.

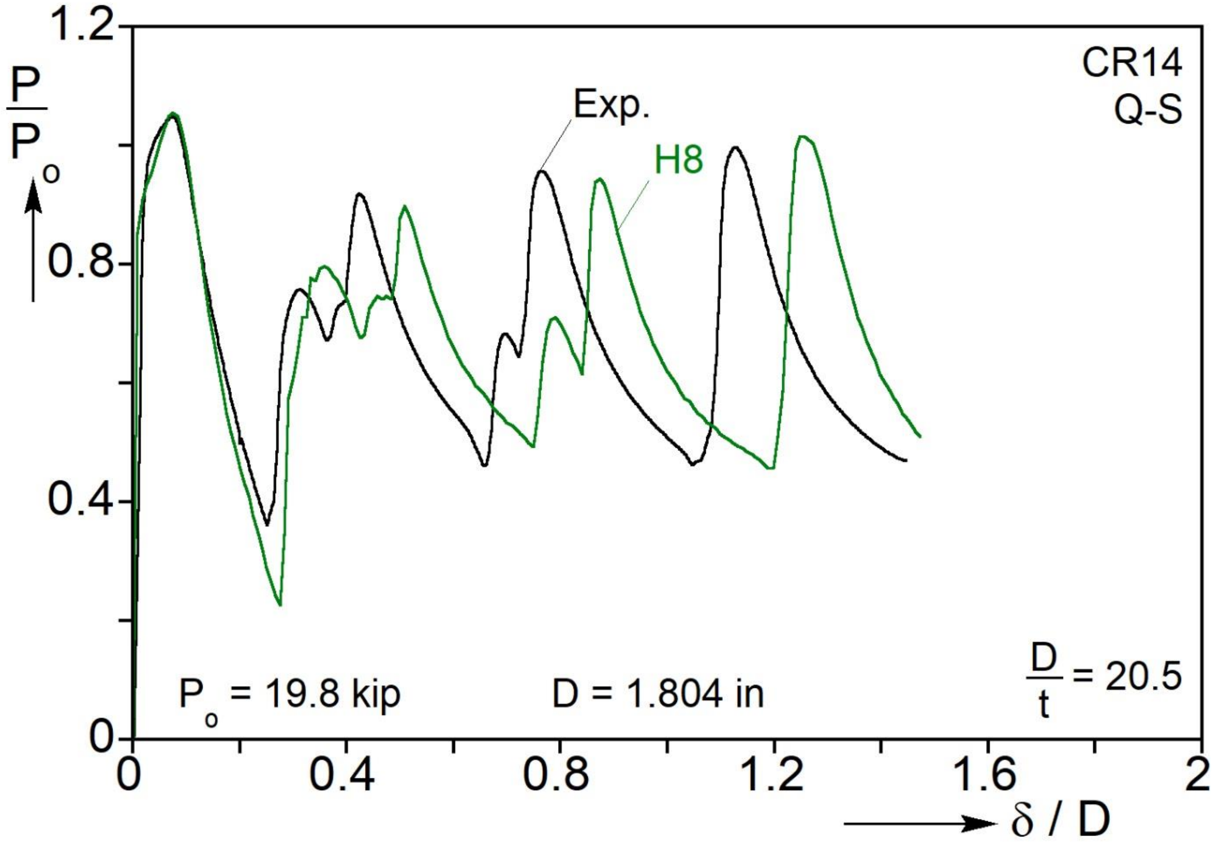

Fig. 4.5: Force-displacement crushing response of experiment and simulation of CR14 using H8 model.

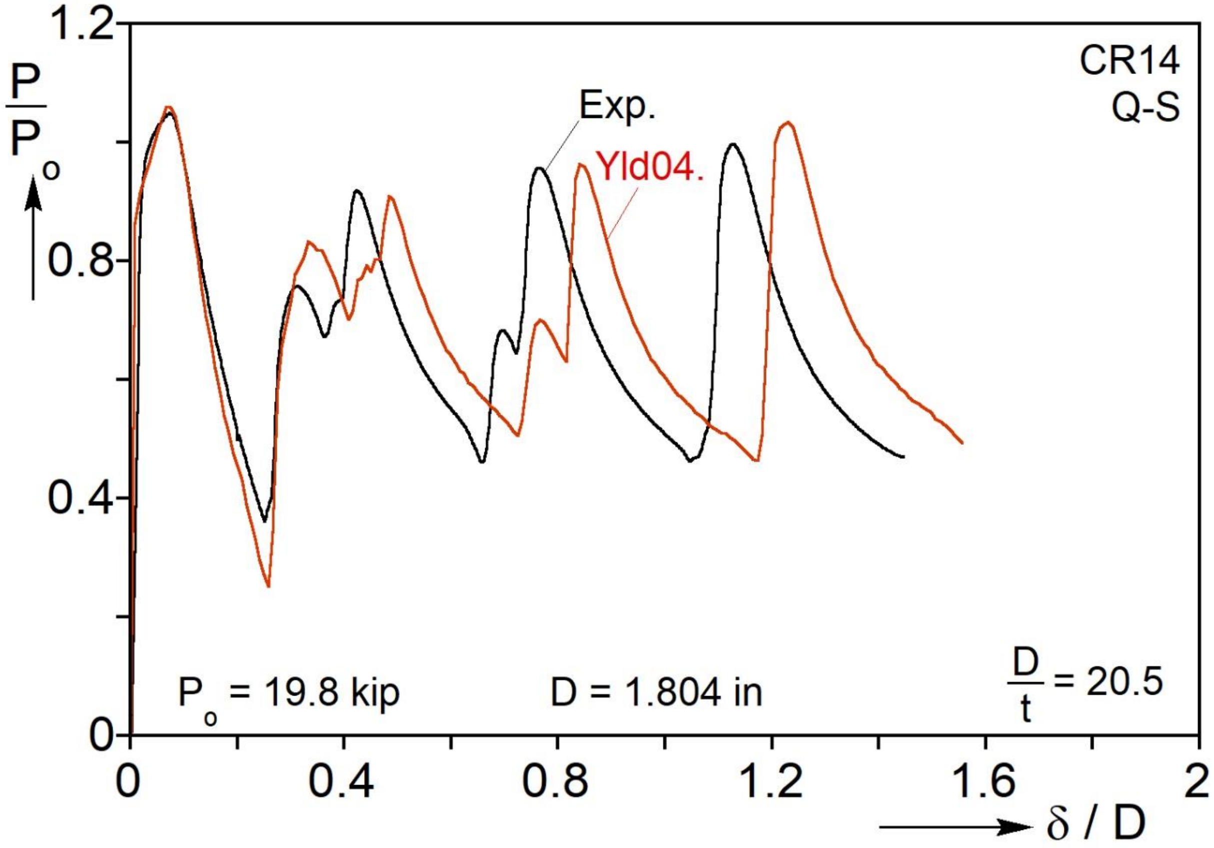

Fig. 4.6: Force-displacement crushing response of experiment and simulation of CR14 using Yld04-3D.

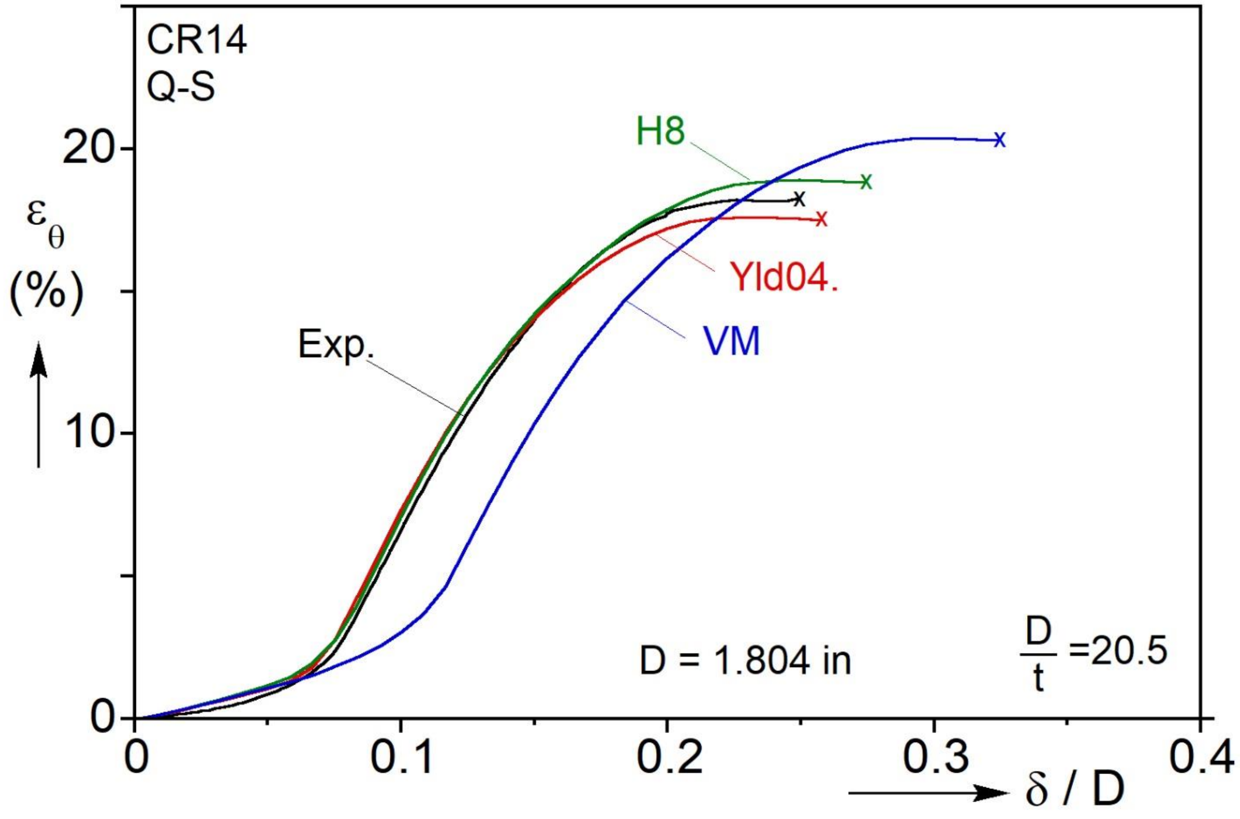

Fig. 4.7: Measured hoop strain-displacement response from the first fold of CR14 together with predictions using VM, H8, and Yld04-3D models.

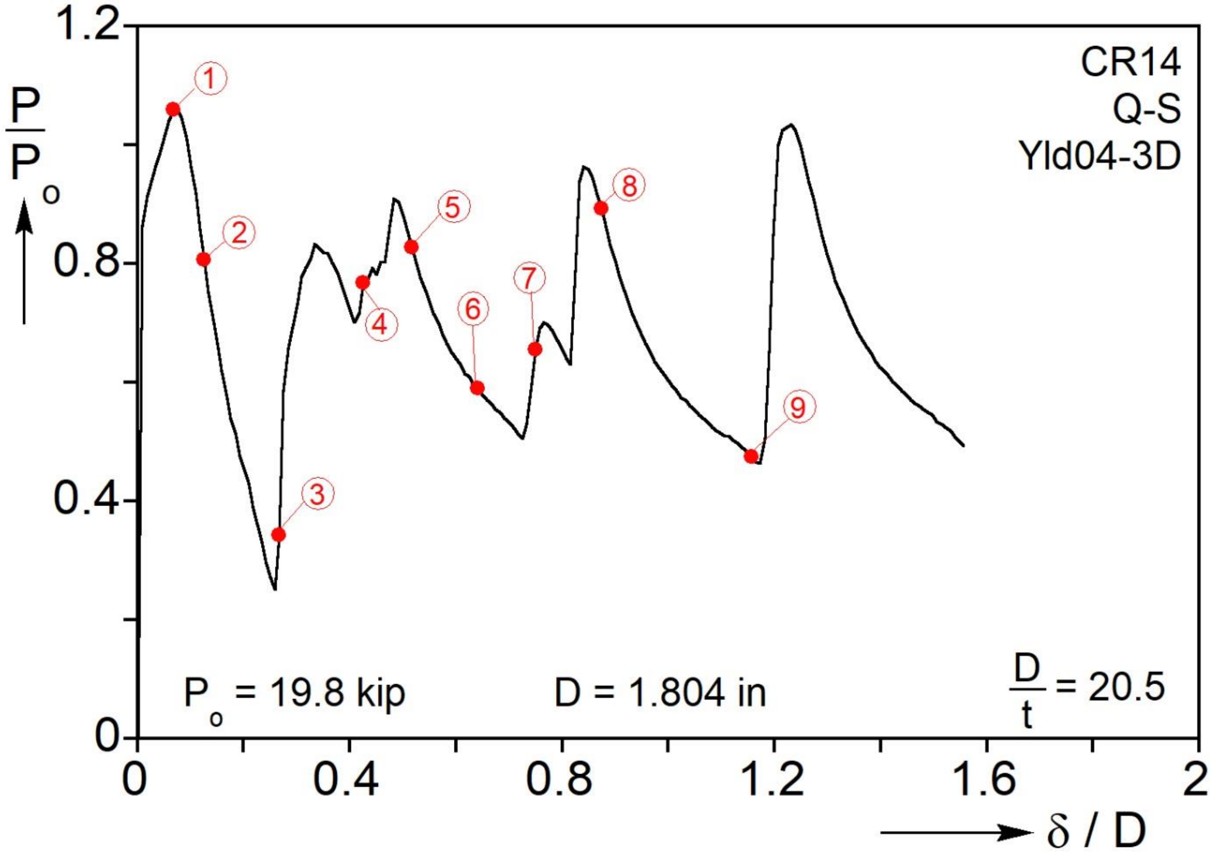

Fig. 4.8: Force-displacement quasi-static crushing response of the simulation of experiment CR14 using Yld04-3D marked with points of interest corresponding to Fig. 4.9.

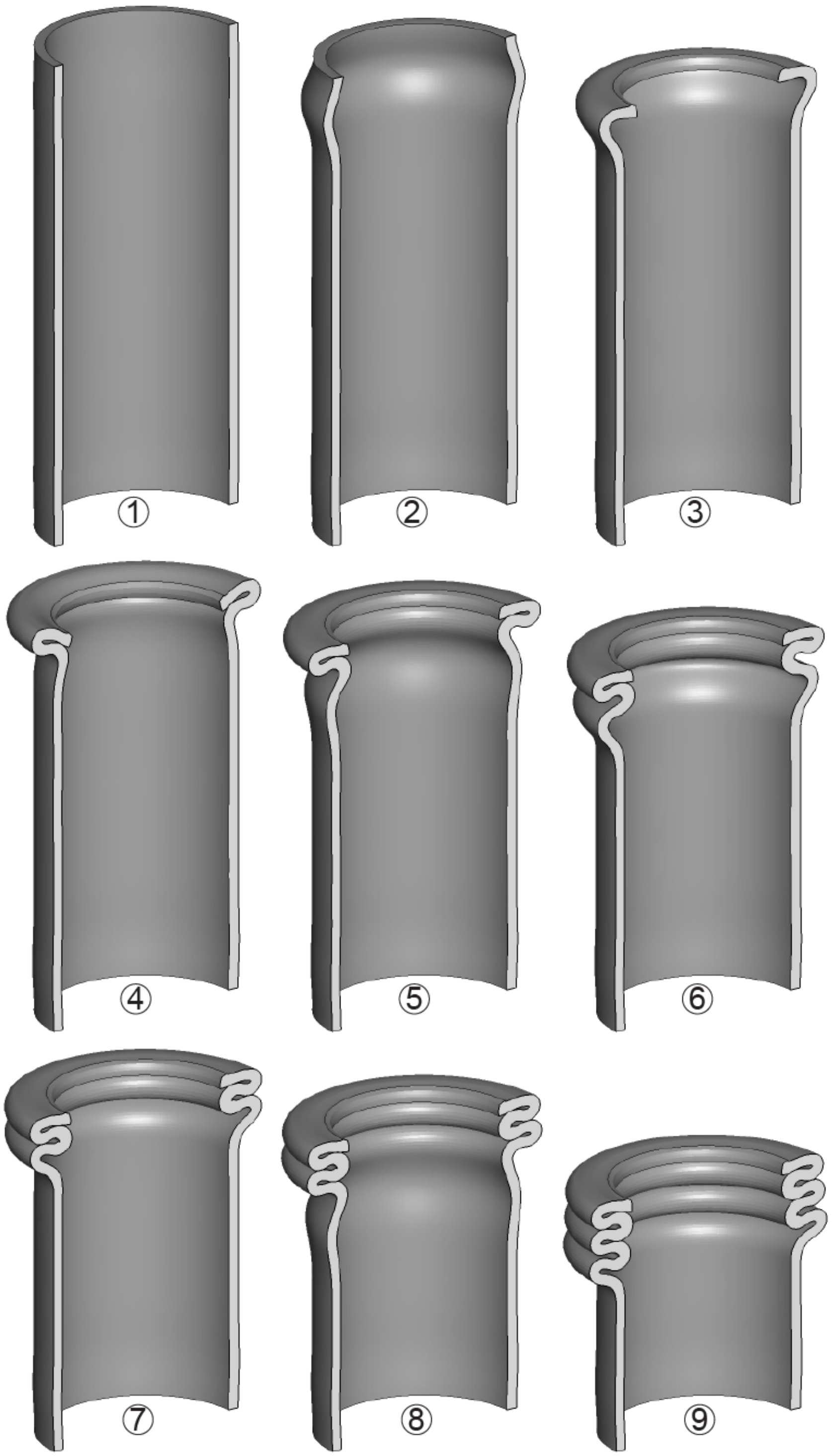

Fig. 4.9: Sequence of crushing configurations showing evolution of axisymmetric folding corresponding to the numbered bullets on the response in Fig. 4.8.

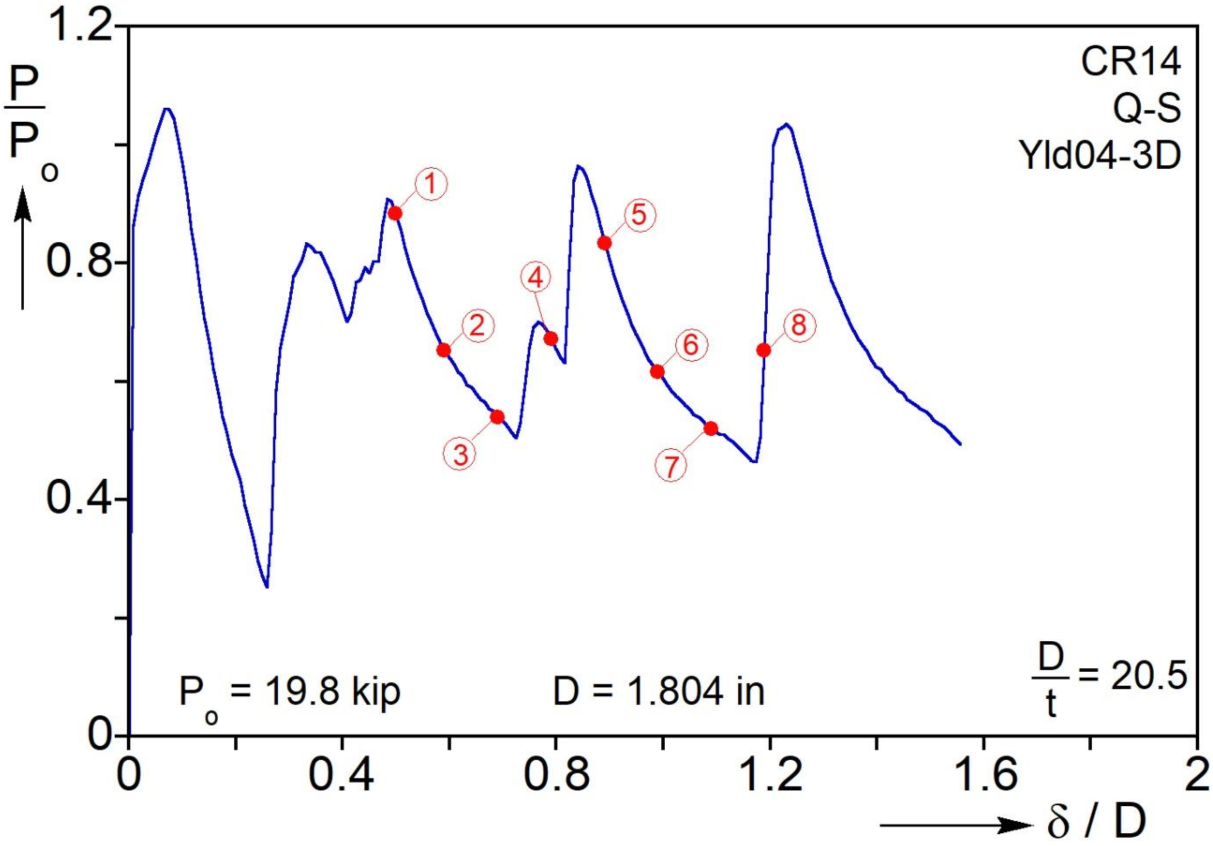

Fig. 4.10: Force-displacement crushing response of CR14 simulation that is used to follow the evolution of the second and third folds in Fig. 4.11.

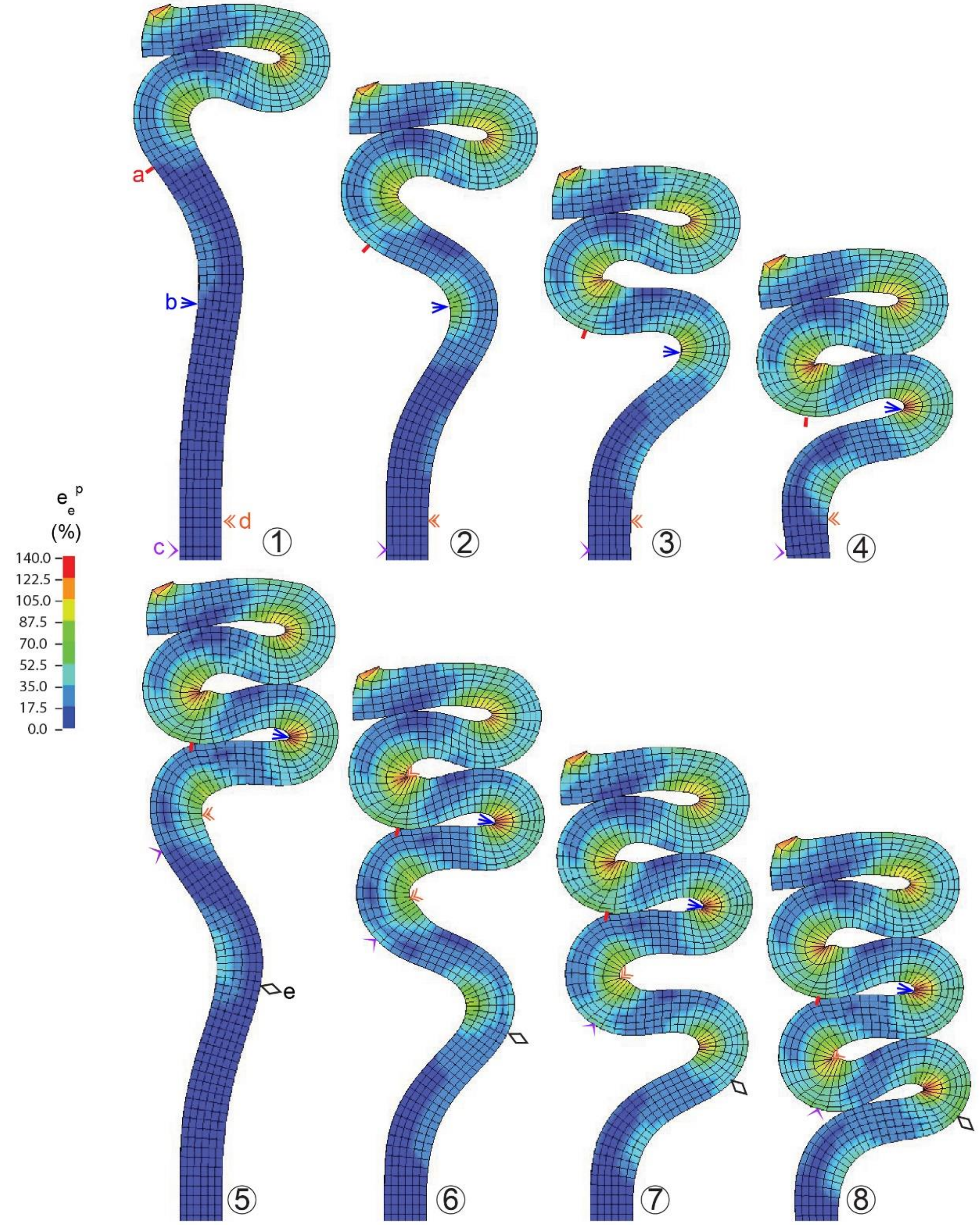

Fig. 4.11: Deformed cross-sections corresponding to numbered bullets in Fig. 4.10 with superimposed equivalent plastic strain contours. Sites marked with symbols and labels a-e correspond to undeformed x/L positions in Figs. 4.12, 4.13.

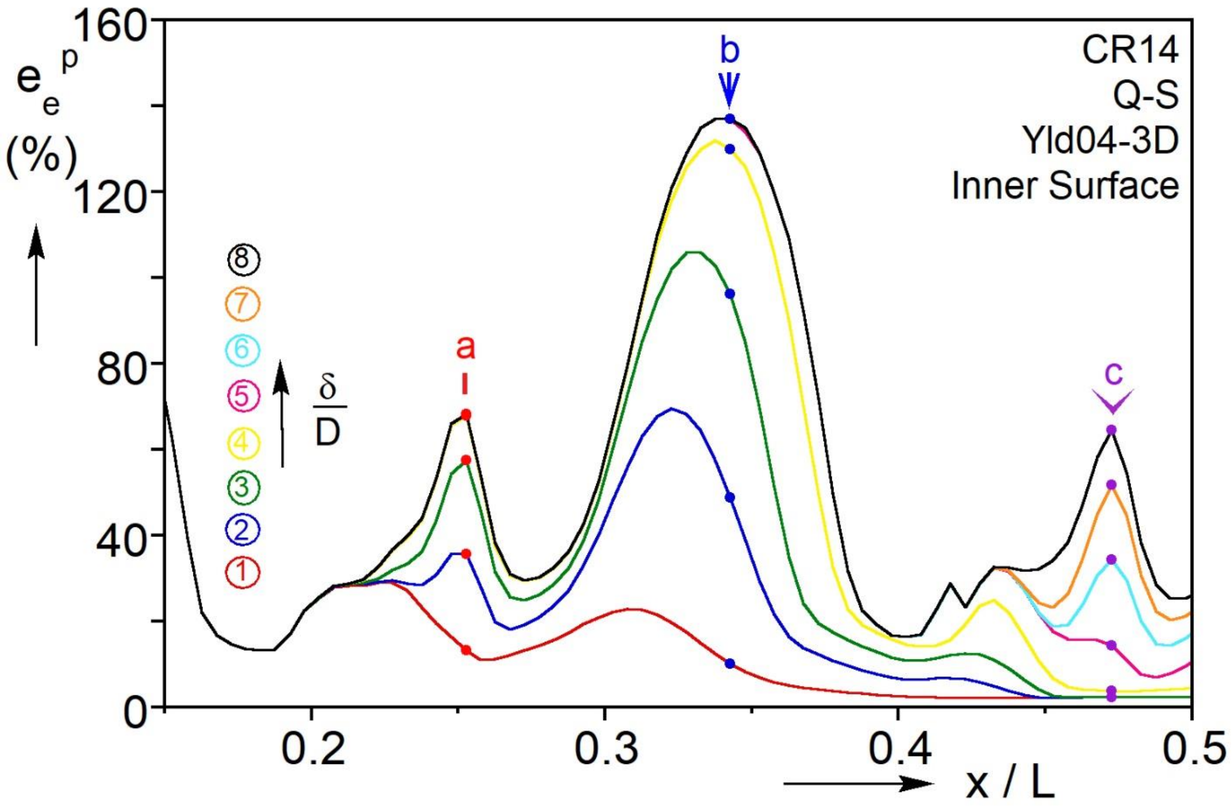

Fig. 4.12: Equivalent plastic strain predictions for the inner surface elements along the undeformed length of the tube. *δ/D* stations correspond to Figs. 4.10, 4.11. Symbols a, b & c correspond to sites that undergo the largest strains (identified in Fig. 4.11).

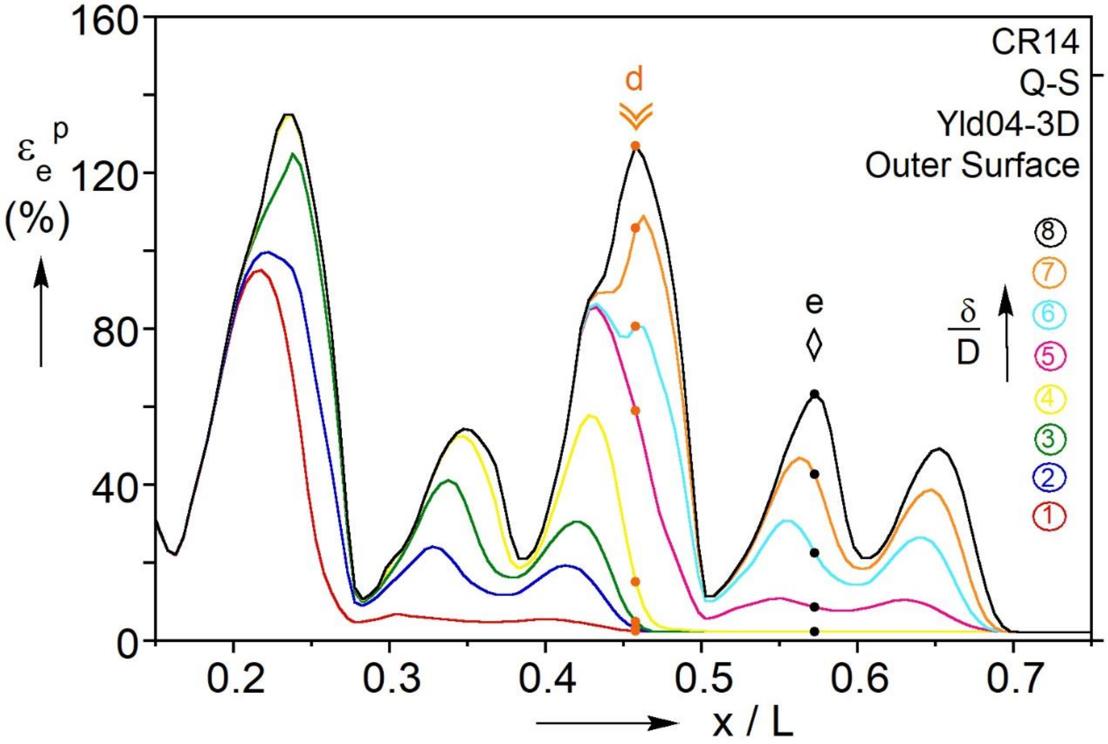

Fig. 4.13: Equivalent plastic strain predictions for the outer surface elements along the undeformed length of the tube. *δ/D* stations correspond to Figs. 4.10, 4.11. Symbols d & e correspond to sites that undergo the largest, unique strain path during the *δ/D* range (identified in Fig. 4.11)

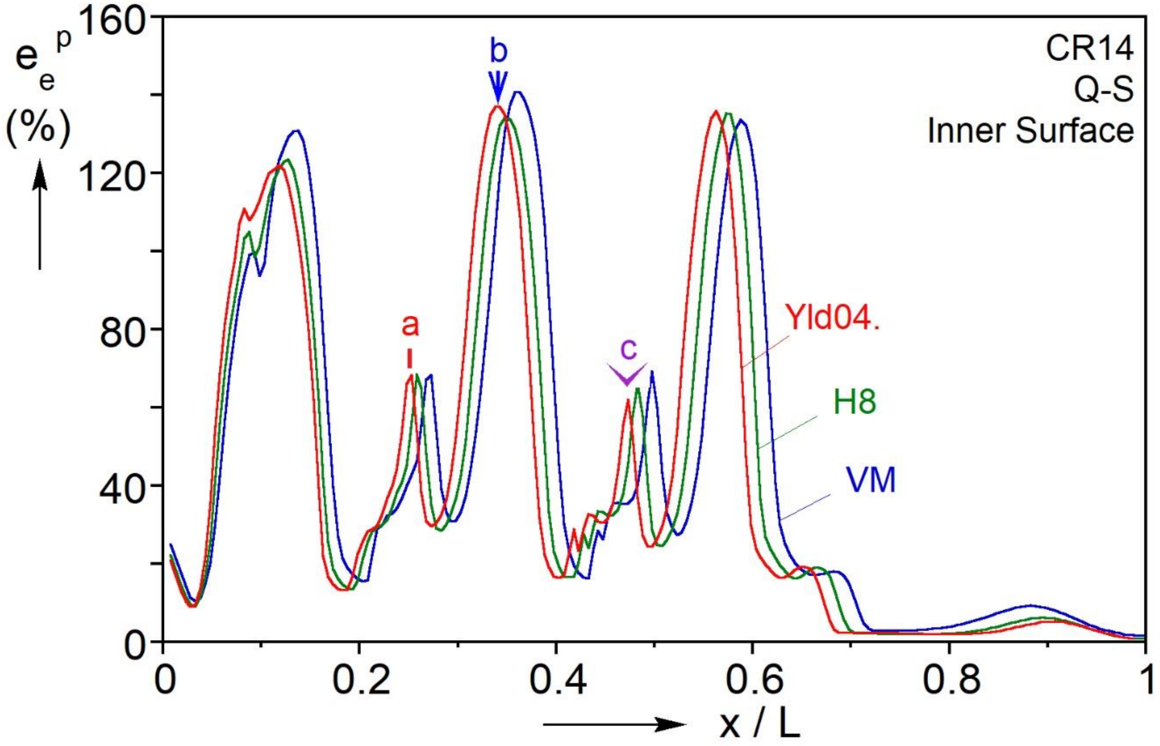

Fig. 4.14: Equivalent plastic strain predictions at the end of the third load cycle for the inner surface elements along the undeformed length of the tube. Sites and symbols a, b, and c correspond to Figs. 4.11, 4.12 and are marked for reference.

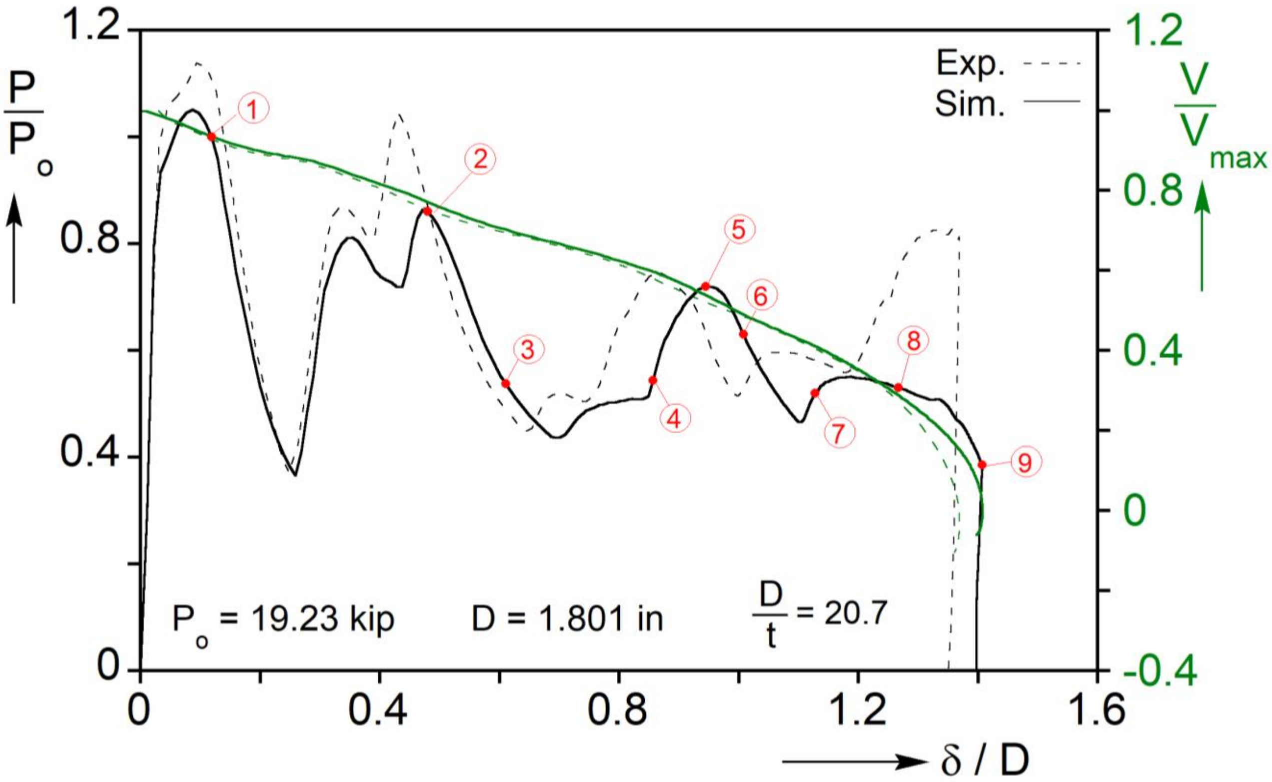

Fig. 4.15: Force-displacement and velocity-displacement responses for experiment DN4. The simulation results are based on Yld04-3D. The marked stations correspond to the configurations in Fig. 4.16. The corresponding experimental responses are drawn with dashed lines.

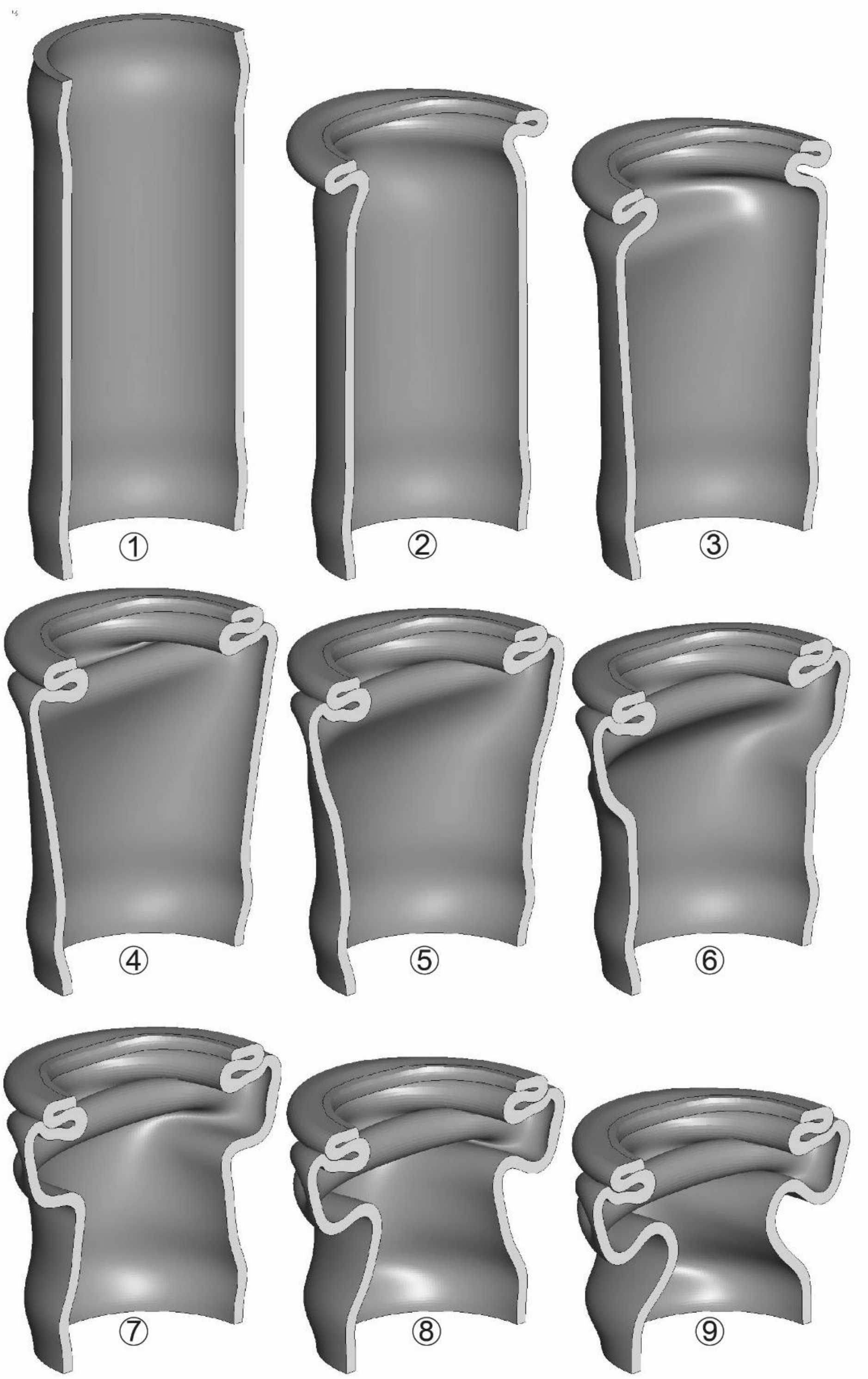

Fig. 4.16: Sequence of crushing configurations showing mode switch from simulation of DN4 corresponding to the numbered bullets on the response in Fig. 4.15.

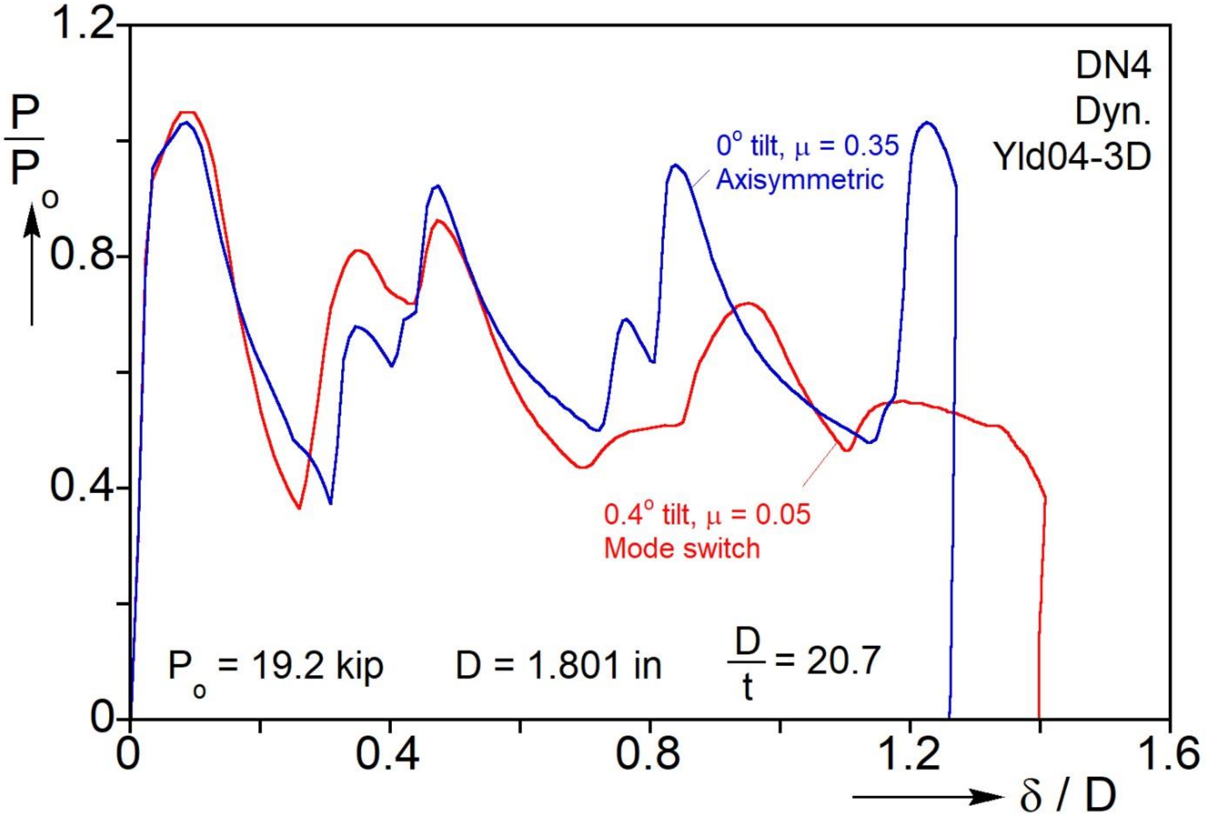

Fig. 4.17: Force-displacement dynamic crushing responses of DN4 from an axisymmetric folding solution and the one that switched to mode-2 folding.

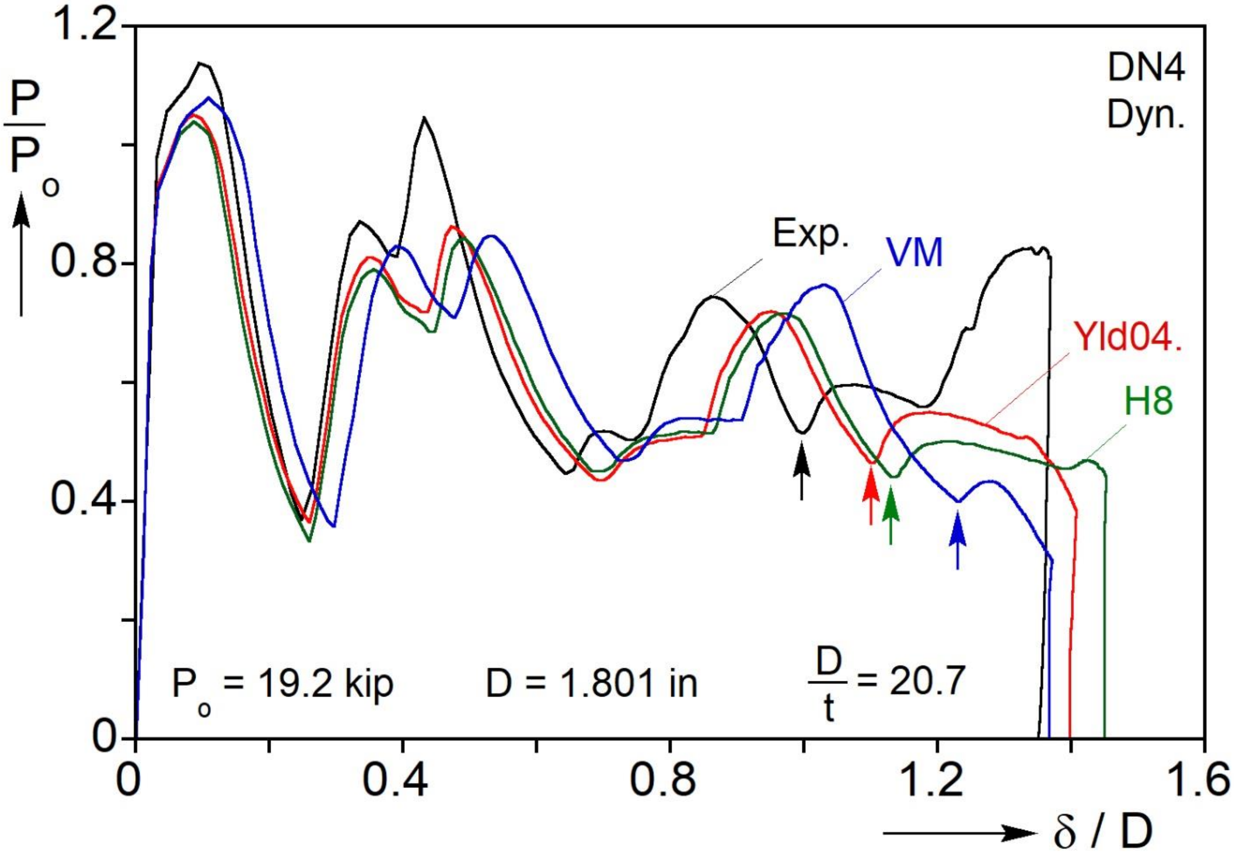

Fig. 4.18: Force-displacement dynamic crushing response of experiment DN4 together with simulation results using VM, H8, and Yld04-3D. The arrows mark the end of the mode-2 loading cycle.

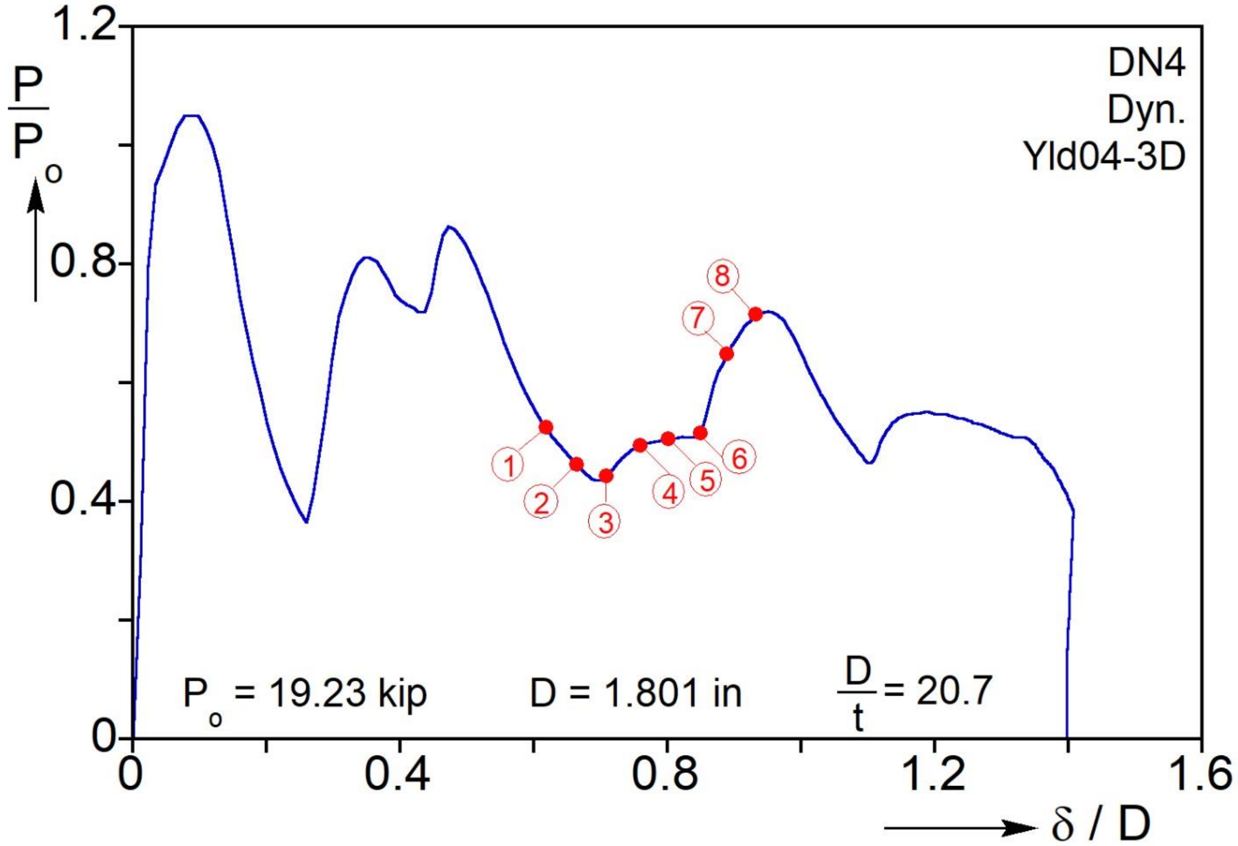

Fig. 4.19: Force-displacement crushing response of DN4 simulation that is used to explain the tearing that occurs in the experiment using the results in Fig 4.20.

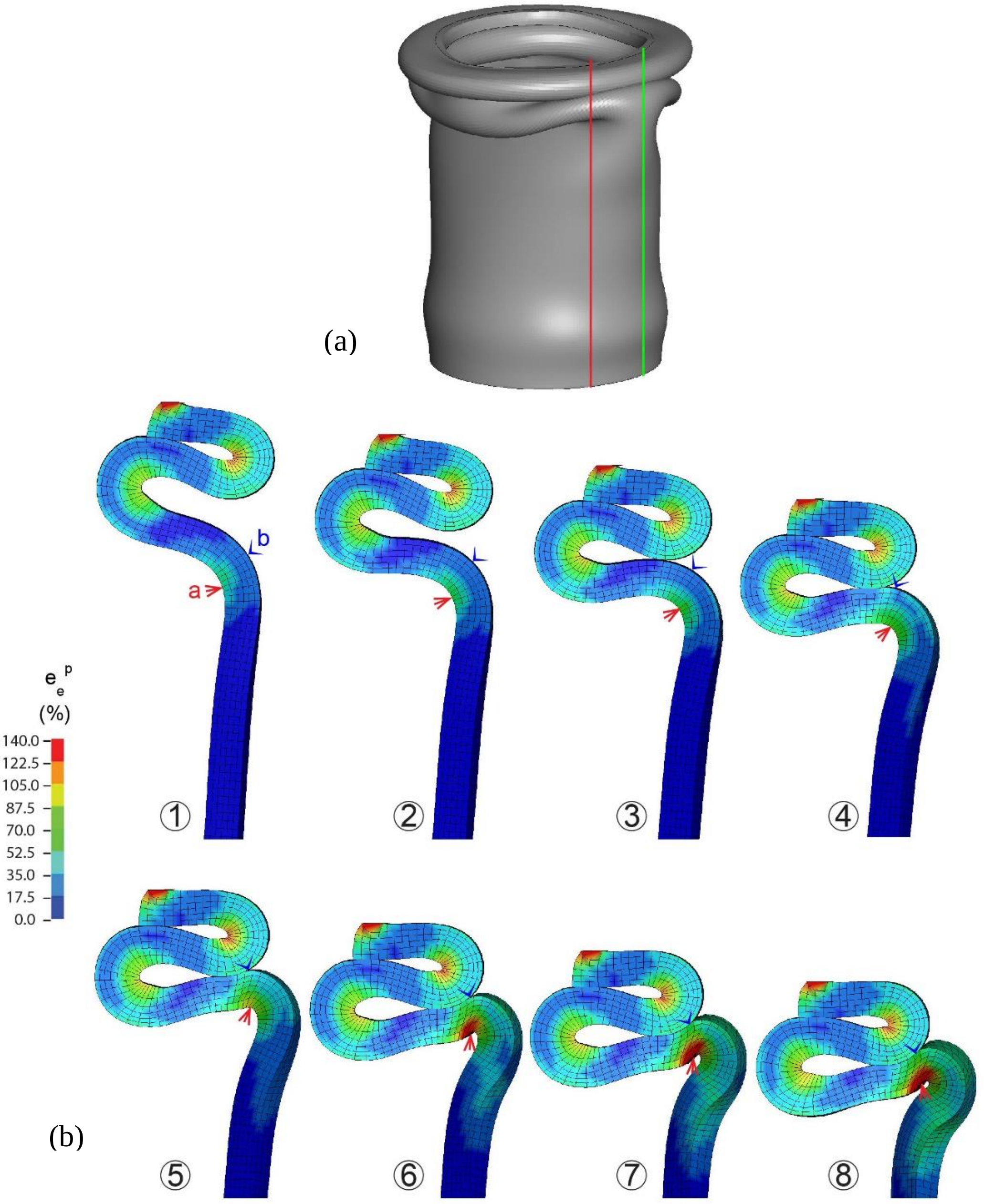

Fig. 4.20: Simulation of crushing of DN4 tube using Yld04-3D. (a) Complete crushed configuration with green line marking the mid-point of the mode-2 fold. (b) Deformed sections along the red line drawn in the full image in (a). The images correspond to the numbered bullets in the response in Fig. 4.19; equivalent plastic strain contours are superimposed. Sites marked with symbols and labels a & b correspond to undeformed *x/L* positions in Figs. 4.21, 4.22.

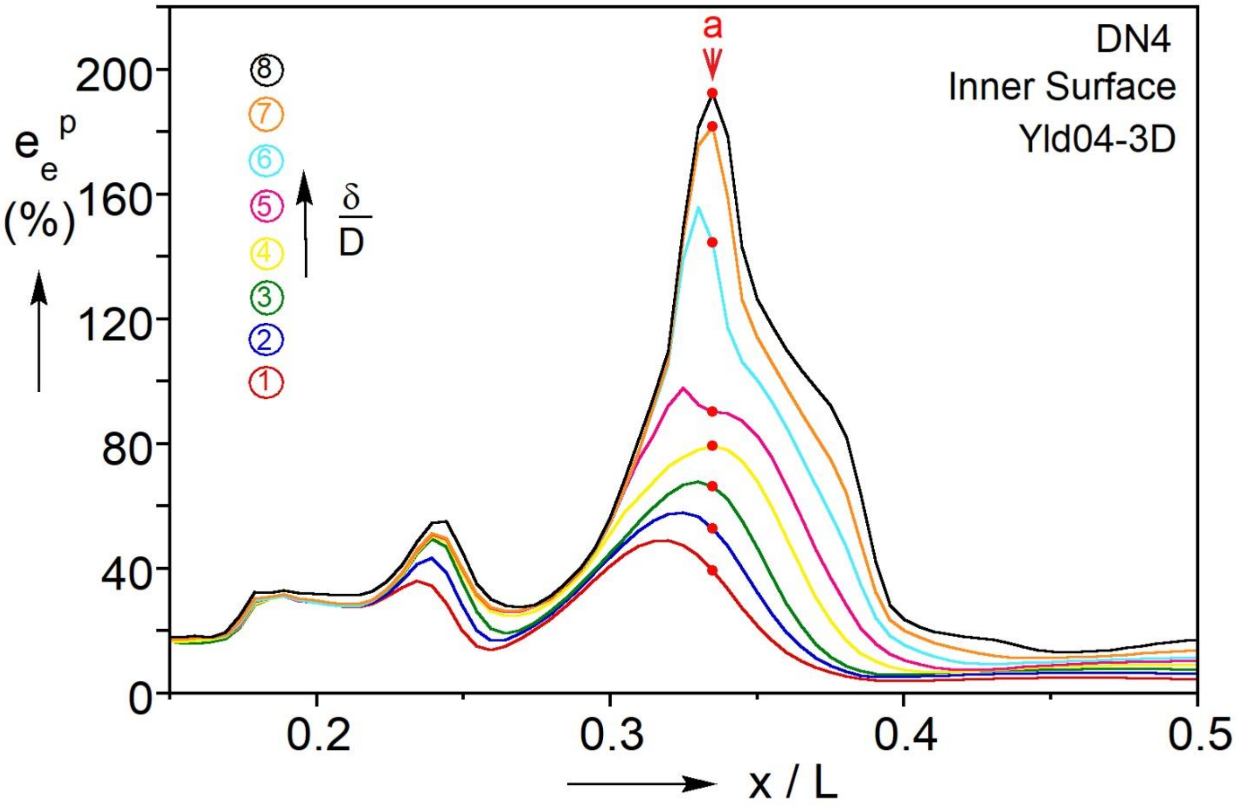

Fig. 4.21: Equivalent plastic strain predictions for the inner surface elements along the undeformed length of the tube. *δ/D* stations correspond to Figs. 4.19, 4.20b. Symbol a corresponds to sites marked on Fig. 4.20b.

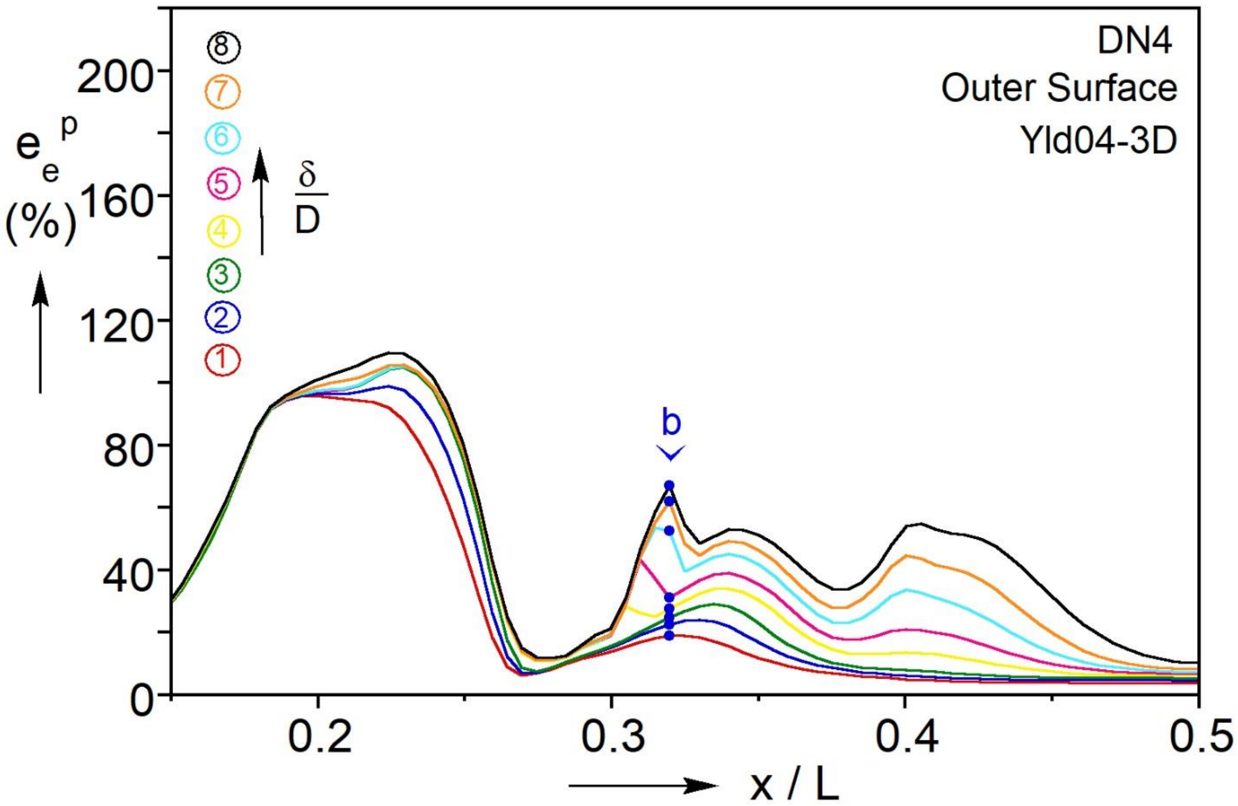

Fig. 4.22: Equivalent plastic strain predictions for the outer surface elements along the undeformed length of the tube. *δ/D* stations correspond to Figs. 4.19, 4.20b. Symbol b corresponds to site marked on Fig. 4.20b.

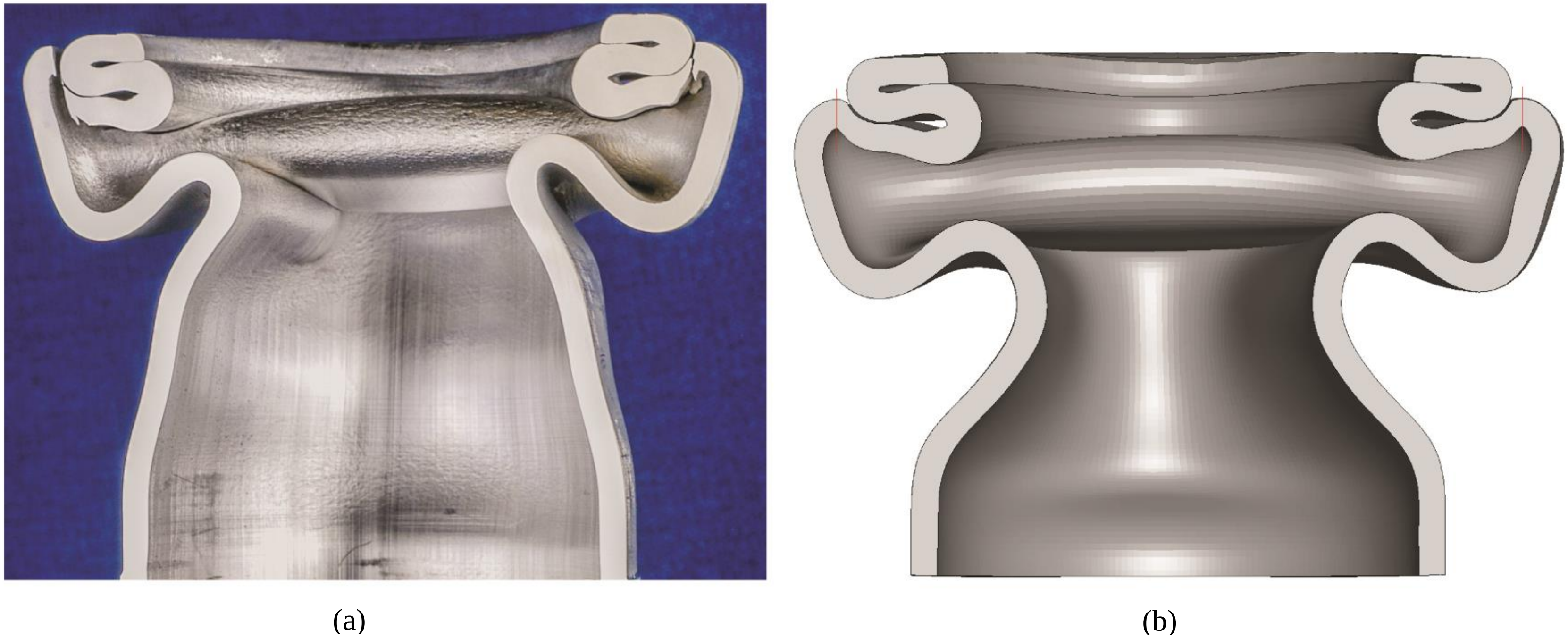
(a) (b)

Fig. 4.23 Cross-sections of DN4 tubes showing the axisymmetric and mode-2 folds. (a) Photograph from the experiment showing the protrusion that has torn through the thickness. (b) Image from Yld04-3D simulation with red lines marking areas of highest strain.

Chapter 5: Conclusions

Closed-section tubes are known to be effective energy absorbing structural components. Aluminum-alloy tubes, preferred for the weight savings they provide, are more challenging due to the low ductility and more complicated constitutive behavior of the alloys. This study used experiment and modeling to investigate the axial crushing and failure of circular Al-6061-T6 tubes. Tubes of different *D/t* ratios were crushed under quasi-static and impact loadings. The crushing resulted in axisymmetric, mode-2, and mode-3 concertina folding. Failure was observed in most of the experiments with the severity depending on the *D/t* and the mode of folding. Three-dimensional nonlinear finite element analysis was used to simulate both types of crushing experiments. The role of the constitutive model on the calculated responses was evaluated using the von Mises, the non-quadratic Hosford, and the anisotropic Yld04-3D models. Numerical crushing simulations using the different constitutive models are compared to measured results. The following main conclusions can be drawn from the study:

Experiments

- The series of quasi-static and dynamic crushing experiments captured the energy absorbing characteristics of thin-walled extruded Al-6061-T6 circular tubes. The structures analyzed were found to be effective energy absorbing devices. However, as expected, some failures were observed in nearly all experiments.
- In most of the quasi-static experiments, moderately thick tubes crushed in an axisymmetric pattern. Some higher *D/t* tubes switched to mode-3 folding.
- In axisymmetric folding, failure typically occurred on the extrados of inside folds. Generally, as the *D/t* decreases, the failure at these sites became increasingly more severe, affecting more of the wall thickness. In the case of higher *D/t* tubes that switched to mode-3, the failure occurred during the development of the mode-3 folds.
- For the dynamic experiments, none of the tubes crushed in a fully axisymmetric fashion. For lower *D/t* tubes, following one or more axisymmetric folds, the crushing switched to mode-2.

For higher *D/t*, tubes switched to mode-3 folding. This consistent mode switch is suspected to be due to small misalignment between the impactor and the top surface of the tube caused by rocking of the yoke that carries the impactor.

- Generally, failures associated with mode-2 and mode-3 folding under dynamic impact were more severe than failures observed in the axisymmetric folding under quasi-static loading.

Numerical Results

- The quasi-static simulations predicted the structural response with good accuracy using the von Mises, Hosford-8, and calibrated Yld04-3D constitutive models. However, each model exhibited a lag in the force-displacement response that was suspected to be from the perfectly plastic extrapolation of the stress-strain at large strains. Of the three, the Yld04-3D was the most accurate when compared to the measured response. The Hosford-8 model was fairly accurate and the von Mises model was the least accurate.
- For quasi-static axisymmetric folding, the Yld04-3D results were used to monitor the strains induced in the evolution of folding. The analysis predicted large tensile strains on the inner extrados at the sites where failure was observed in the experiments. The location of the predicted highest strain corresponds well with the location where the tensile failure took place. It is worth mentioning that very high compressive strains were recorded on the compressed sides of the folds.
- In the simulation of dynamic crushing, the mode-switch observed in the experiments was reproduced by the introduction of a small amount of misalignment between the impactor and the tube. The misalignment parameters had to be determined empirically in order to closely match the experimental response.
- The dynamic structural response was predicted fairly well by all constitutive models. The Yld04-3D was again the most accurate. However, this model somewhat under predicted the initial load peak and the subsequent axisymmetric load peaks when compared to the measured response. In the dynamic crushing results presented, severe failure developed during the formation of the second mode-2 fold. The simulation and the measured response deviate during

the part of the response when failure took place in the experiment. The experiment traces an additional load peak whereas the simulation begins to unload before a new load peak can be traced, as in the absence of failure the available kinetic energy has been depleted. This difference can only be addressed by adopting a model that includes a failure criterion followed by a failure tracking scheme such as element deletion.

- In the case of the mode-2 folding, the maximum strains predicted using the Yld04-3D model occur close to locations where failure was observed in the experiments. The maximum strains were very large on the inside surface elements while on the outside surface elements were lower. This suggests that in the experiment the tearing failure may have initiated on the inside surface of the tube but, again, this can only be confirmed by adopting an appropriate failure criterion into the model.
- Since tearing during crushing can result in catastrophic failure of important structural components, the tracking of tearing failures is most important. Such an effort requires a dependable failure criterion coupled with a method like element deletion.

Appendix A: Definition of Crushing Parameters

The definitions of crushing parameters are presented using a generic force-displacement load response of an axisymmetric experiment shown in Fig. A.1. The yield load, P_0, is defined as

$$P_0 = \sigma_0 \cdot \pi \cdot D \cdot t \tag{A.1}$$

where σ_0 is the yield stress taken from a uniaxial tension test on a dogbone specimen and D and t are the diameter and wall thickness of the tube. For this Al-6061-T6 material, the yield stress was found to be 39.7 ksi using a 0.2% offset method.

The limit load, P_L, is the maximum load of the initial load peak. The mean crushing load, $\bar{P}$, is the average load across the P-δ response.

For axisymmetric folding, $\bar{P}_{2-3}$ represents the mean crushing load over two steady-state periods. It has the subscript 2-3 because the steady state cycles chosen are typically the second and third cycles. For the quasi-static experiments, there were generally two well-defined steady state loading cycles. As mentioned in Chapter 2, CR12 and CR16 did not crush in a fully axisymmetric fashion. For CR12, this mode switch occurred too early and thus there were not two well defined steady-state regions of the load response. CR16 switched modes but the switch occurred just after the second steady state load cycle. For the dynamic experiments, the mode switch occurred just after the first steady state loading cycle.

δ_{cr} represents the maximum crushing displacement of the hydraulic cross-head in quasi-static experiments, or the drop weight assembly impactor for dynamic crushing experiments.

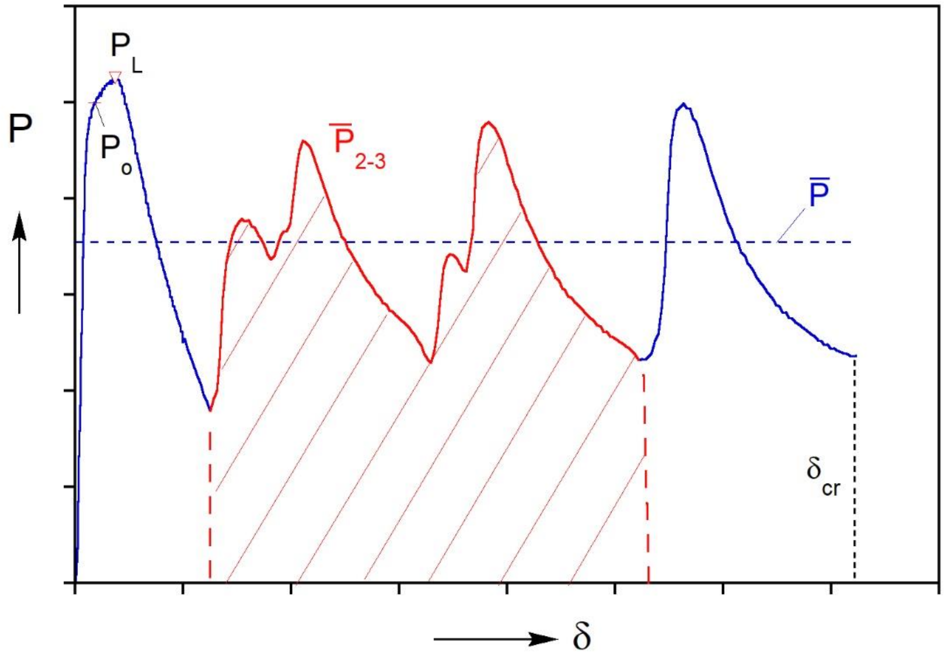

Fig. A.1: Typical axisymmetric crushing response with annotated descriptions of loading parameters.

References

Abramowicz, W., Jones, N., 1984. Dynamic axial crushing of circular tubes. *International Journal of Impact Engineering*. **2**, 263–281.

Ayapana, Erick. "15 Automotive Aluminum Warriors - Motor Trend." MotorTrend, MotorTrend, 26 Feb. 2015, www.motortrend.com/news/15-automotive-aluminum-warriors/.

Alexander, J. M. (1960). An approximate analysis of the collapse of thin cylindrical shells under axial loading. *The Quarterly Journal of Mechanics and Applied Mathematics.* **13(1)**, 10-15.

Bardi, F., Yun, H.D., Kyriakides, S. 2003. On the axisymmetric progressive crushing of circular tubes under axial compression. *International Journal of Solids and Structures.* **40**, 3137-3155.

Barlat, F., Aretz, H., Yoon, J.W., Karabin, M.E., Brem, J.C., Dick, R.E. (2005). Linear transformation-based anisotropic yield functions. *International Journal of Plasticity*. **21**, 1009-1039.

Chen, K., Scales, M., Kyriakides, S. (2018). Material hardening of a high ductility aluminum alloy from a bulge test. *International Journal of Mechanical Sciences. Sciences.* **138-139**, 476-488.

Chen, K., Scales, M., Kyriakides, S. (2019). Material response, localization and failure of an aluminum alloy under combined shear and tension: Part II analysis. *International Journal of Plasticity*. **120**, 361-379.

Giagmouris, T., Kyriakides, S., Korkolis, Y.P., and Lee, L.-H. (2010). On the localization and failure in aluminum shells due to crushing induced bending and tension. *International Journal of Solids and Structures.* **47**, 2680-2692.

Hosford, W.F. (1972). A generalized isotropic yield criterion. *ASME Journal of Applied Mechanics*. **39**, 607-609.

Kazancı, Z., Bathe, K., 2011. Crushing and crashing of tubes with implicit time integration. *International Journal of Impact Engineering*. **42**, 80-88.

Kohar, C. (2017). Multi-scale Modeling and Optimization of Energy Absorption and Anisotropy in Aluminum Alloys. UWSpace. http://hdl.handle.net/10012/11759.

Kohar, C., Brahme, A., Imbert, J., Mishra, R., Inal, K., 2017. Effects of coupling anisotropic yield functions with the optimization process of extruded aluminum front rail geometries in crashworthiness. *International Journal of Solids and Structures*. **128**, 174-198.

Krome, Charles. "Unibody vs. Body on Frame: What's the Difference?: CARFAX Blog." CARFAX, 19 June 2018, www.carfax.com/blog/unibody-vs-body-on-frame-construction.

Kyriakides, S., Corona, E. *Mechanics of Offshore Pipelines: Volume I.* El Sevier, 2007.

N.H.T.S.A., 2015. Overview of NHTSA Priority Plan For Vehicle Safety and Fuel Economy, 2015 to 2017. N.H.T.S.A., Washington.

Scales, Martin Filipp, and S. Kyriakides. "Localization and Failure of Aluminum 6061-T6 under Biaxial Loading." University of Texas at Austin, 2019.

Singace, A.A., Elsobky, H., Reddy, T.Y., 1995. On the eccentricity factor in the progressive crushing of tubes. *International Journal of Solids and Structures*. **32**, 3589–3602.

Singace, A.A., 1999. Axial crushing analysis of tubes deforming in the multi-lobe mode. *International Journal of Mechanical Sciences.* **41**, 865-890.

Tardif, N., Kyriakides, S. (2012). Determination of anisotropy and material hardening for aluminum sheet metal. *International Journal of Solids and Structures*. **49**, 3496-3506.

Wierzbicki, T., Bhat, S.U., Abramowicz, W., Brodkin, D., 1992. Alexander revisited—A two folding elements model of progressive crushing of tubes. *International Journal of Solids and Structures.* **29**, 3269–3288.

Wilbert, A., Yang, W.-Y., Kyriakides, S., Floccari, J.F., 2010. Buckling and progressive crushing of laterally loaded honeycomb. *International Journal of Solids and Structures*. **48**, 803-816.

Vita

Jake Haley was born in Memphis, TN and raised in Kossuth, MS. He graduated from Kossuth High School in 2012 and subsequently graduated from Mississippi State University in December 2016 with a B.S. in Mechanical Engineering. He entered the Graduate School at The University of Texas at Austin in 2017 to pursue a M.S. in Engineering Mechanics.

Permanent email: jakeandrewhaley@gmail.com

This thesis was typed by the author.